Mathematical Modeling of Copper and Brass Upcasting

K. HÄRKKI and J. MIETTINEN

A study has been performed to establish basic knowledge in heat transfer and solidification for copper and brass upcasting. The study combined pilot scale measurements, mathematical modeling, and metallographic examination of the cast rod samples. The pilot scale measurements involved temperature measurements with several thermocouples inserted in the copper jacket of the mold. Temperature measurements of the surface of the cast rod were carried out as well. A three-dimensional (3-D) mathematical model of the copper mold and graphite die was constructed to characterize the heat flux profiles quantitatively from the measured mold temperature data. The heat flux was observed to have a maximum value near the first contact point between the copper mold and the graphite die and to decrease rapidly with increasing distance up to the mold. The calculated heat flux profiles were used as boundary conditions for another mathematical model, which calculated temperature profiles in the cast rod. A model for estimation of material data and microstructure was used for simulating the thermophysical data needed in the calculations and to predict certain microstructural properties in the cast rods. The calculated surface temperatures of the cast rod at the mold exit agreed well with the measured temperature values. Also, the calculated microstructural properties, such as secondary dendrite arm spacing, phase distribution, and microsegregation of zinc, were in good agreement with the measured ones.

I. INTRODUCTION

CONTINUOUS casting of copper and brass bars and rods generally used for the production of drawn wire can be accomplished by different commercial methods. In the wheel and the belt methods,[1] the casting machine consists of a casting wheel with a machined groove of desired configuration forming three sides of the casting cavity. A continuous steel band closes with the wheel, forming the fourth side of the mold. In the Outokumpu Upcast system,[2] solidification occurs inside a submerged die after which the solid rod is pulled vertically upward. The main advantages of the Upcast process over other methods of producing copper and brass wire rod are (1) the melt feeding can be controlled easily and accurately; (2) the Upcast production line is a multistrand unit, which gives flexibility in meeting the required capacity; (3) the coolers, including the graphite die, are individually changeable, so that a change of one cooler does not disturb other strands; and (4) it is possible to cast different strand shapes and sizes with the same casting furnace.

Primarily, the casting of copper or brass can be considered as a heat extraction process. The conversion of molten metal into a solid metal rod involves removal of superheat and latent heat of solidification. The liquid metal is solidified in a mold, which is the most critical and essential component of the continuous casting equipment. Heat transfer in the mold is one of the main factors limiting the maximum productivity. With higher casting speeds, more heat is transported into the mold and thus the heat transfer from the rod to the mold has to increase in order to solidify the rod in the mold.

Numerous studies concerning continuous casting and its mathematical modeling can be found from the literature.[3–23] Most of these publications, however, deal with the continuous casting of steel rather than the continuous casting of copper and copper-based alloys. In the case of steel, the heat flow along the casting direction is insignificant compared to that along the cross-sectional direction, and can therefore be neglected. This assumption is generally accepted, due to the relatively low thermal conductivity of steel. This means that the conductive heat flow along the casting direction is negligible compared to the convective heat transport due to the casting speed. In copper and brass casting, this assumption is not valid, due to the higher thermal conductivity, and one has to make the simulation three-dimensionally.

The aim of this study was to establish basic knowledge for copper and brass concerning heat transfer and solidification in the mold of the upcasting device. This was achieved through temperature measurements, mathematical modeling, and metallographic evaluation of rod samples. A better understanding of the casting process helps to optimize the casting conditions and, furthermore, to increase the plant productivity. The following experimental and modeling techniques were developed and used.

(1) Temperature measurements on an operating mold were carried out to determine the influence of casting speed on the mold wall temperature distribution.
(2) Temperature measurements of the outgoing cooling water were carried out to determine the influence of casting speed on the outgoing cooling water temperature.
(3) Metallographic analysis was used to examine the cast rod samples.
(4) A three-dimensional (3-D) mathematical model (HTM) was constructed with a commercial program package (FIDAP) to simulate the heat transfer in the mold. The

---

K. HÄRKKI, Research Scientist, formerly with the Laboratory of Metallurgy, Helsinki University of Technology, is with Outokumpu PoriCopper, FIN-28101 Pori, Finland. J. MIETTINEN, Research Scientist, is with the Laboratory of Metallurgy, Helsinki University of Technology, FIN-02015 Espoo, Finland.

Manuscript submitted March 31, 1998.

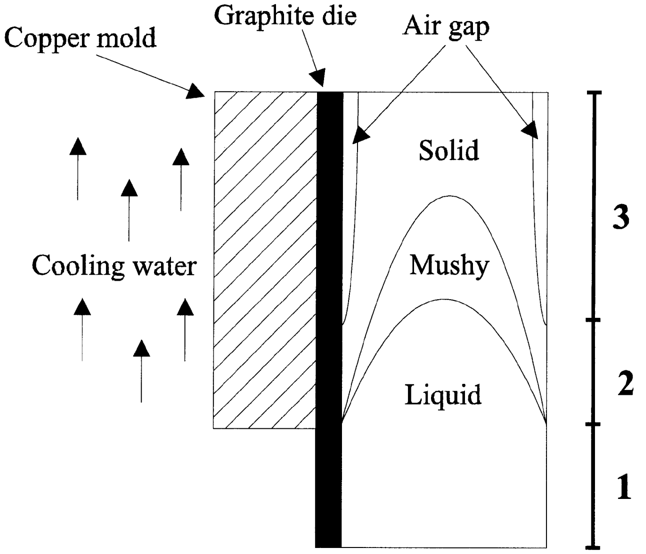

Fig. 1—Schematic presentation of the interface between the casting and the mold.

model was used to convert the measured temperature data of item 1 to heat fluxes needed in the second stage of modeling (item 5).

(5) An axisymmetric mathematical model (HTR) was also constructed with FIDAP to simulate the heat transfer and solidification in the cast copper and brass rods. The heat fluxes evaluated with the HTM model were used in the HTR model as boundary conditions).

(6) A model for material data and microstructure (MDM) was developed and used to simulate the thermophysical data needed in the calculations of the HTR model and to predict certain microstructural properties in the cast rods.

II. HEAT TRANSFER PHENOMENA

Heat transfer can be considered to be the major phenomenon in a continuous casting process. Consequently, it is one of the limiting factors in the operation of a caster. Heat transfer not only limits the maximum productivity, but it also profoundly influences the quality. So, it is clear that the control of heat transfer, rather than a simple maximization of heat extraction, is the key element of good casting practice for the production of high quality copper and brass rod.

The heat flow is rather complicated, because it is primarily controlled by the formation of an air gap separating the mold from the cast copper or brass rod. The location and size of the gap are simultaneously influenced by the shrinkage of the shell and the metallostatic pressure exerted by the liquid pool. The interface between the casting and the mold can be divided into three zones, as shown in Figure 1:

(1) the zone where liquid metal is in contact with the mold;

(2) the zone where the solid shell is formed and is not yet pulled away from the mold; and

(3) the zone where an air gap exists (as a consequence, heat transfer is greatly reduced).

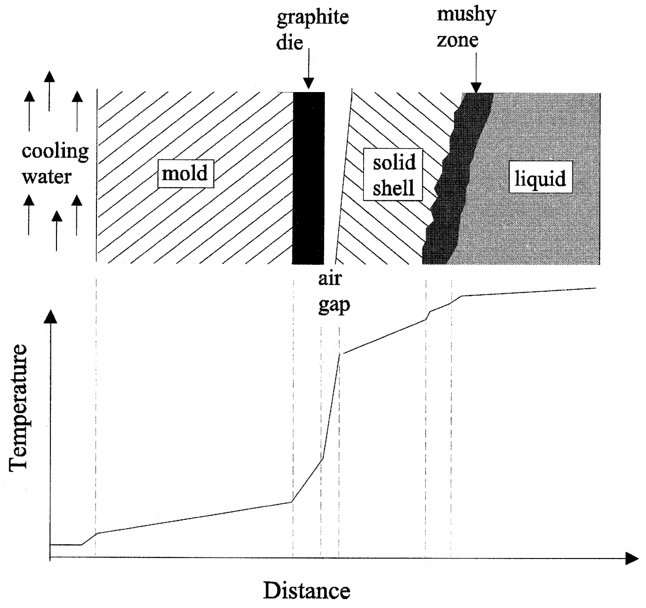

Fig. 2—Schematic presentation of temperature across an upcast mold and cast brass.

In the bottom part of the cooler, there is contact between the liquid metal and the lower part of the mold, which is not cooled. Above it, there is the water-cooled part of the mold, inside which solidification starts with the formation of a solid shell against the graphite die. The liquid pool is quite short in the case of pure copper, with very high thermal conductivity. With brass having a mushy zone and lower thermal conductivity, the liquid pool is longer. When solidification proceeds, shrinkage occurs and an air gap is formed between the rod and the mold, constituting the largest single heat flow resistance. In upcasting, its evolution mainly depends on the solidification shrinkage of the cast rod, as the metallostatic pressure is rather small. After the air gap formation, the heat from the liquid metal is transferred to the mold cooling water *via* a series of thermal resistances. Figure 2 shows schematically the temperature distribution across the entire mold and shell.

Heat transfer is controlled by the following:

(1) convection and conduction of liquid superheat to the shell surface;
(2) solidification, which includes latent heat evolution in the mushy zone;
(3) conduction through the solid shell;
(4) conduction, convection, and radiation across an air gap separating the graphite die and the solidified rod;
(5) conduction through the graphite die wall;
(6) conduction through the copper mold wall; and
(7) convection at the copper mold/cooling water interface.

Heat flux from the rod to the mold occurs by radiation, convection, and conduction through the gap that separates the cast metal and the hot face of the graphite. The heat flux, q, transferred by radiation is conventionally given by equation

$$q = \sigma (T_1^4 - T_2^4) \frac{1}{\frac{1}{\varepsilon_1} + \frac{1}{\varepsilon_2} - 1} \qquad [1]$$

where σ is the Stefan–Boltzmann constant ($5.668 \cdot 10^{-8}$ J/m^2 s K), T_1 is the surface temperature of the cast wire rod (in

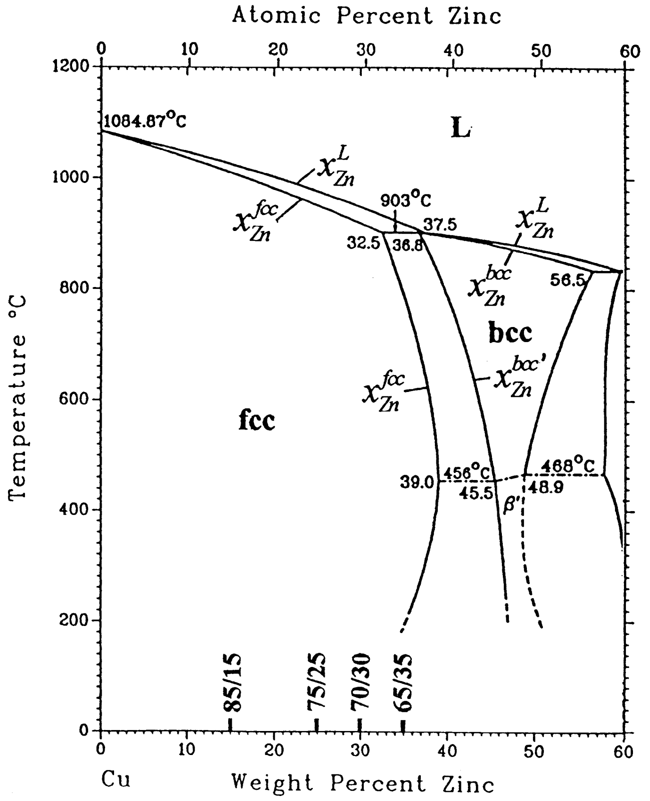

Fig. 3—Phase diagram of the copper-zinc system.[24] The zinc contents of the studied brasses have been marked and important phase interface compositions $x\text{Zn}^{\phi}$ have been added to the diagram.

K), T_2 is the surface temperature of the mold (in K), ε_1 is the emissivity of the cast wire rod, and ε_2 is the emissivity of the graphite die of the mold. Heat flux by conduction and convection in the air gap can be calculated with the equation

$$q = \frac{k_{\text{TOT}} \Delta T}{r_2 \ln \left(\dfrac{r_2}{r_1} \right)} \tag{2}$$

where k_{TOT} is the total thermal conductivity of the air (in W/m K), ΔT is the temperature gradient in the air gap (in Kelvin), r_1 is the radius (in meters) of the cast wire rod, and r_2 is the inside radius (in meters) of the graphite die of the mold. The term k_{TOT} can be described as

$$k_{\text{TOT}} = k_{\text{LAM}} + k_{\text{TUR}} \tag{3}$$

where the term k_{LAM} represents the thermal conductivity when no turbulence is present, and k_{TUR} describes the effect of turbulence on the heat transfer.

Heat exchange between the copper jacket of the mold and the cooling water takes place by convection. Heat flux by convection can be calculated with the equation

$$q = \alpha \, (T_1 - T_2) \tag{4}$$

where α is the heat transfer coefficient (in W/m^2 K), T_1 is the surface temperature of the copper mold (in Kelvin), and T_2 is the temperature of the cooling water (in Kelvin). Heat transfer from the mold to the cooling water is complex, and the heat transfer coefficient depends on many different factors, such as the shape of the mold wall, the type characteristics of the fluid flow (turbulent or laminar), the temperature, and the physical properties of the fluid.

In this work, a temperature boundary condition is used at the mold cooling water side, and hence, the heat transfer coefficient from the mold to the cooling water is not needed. Also, two separate models were constructed to avoid modeling of the air gap formation, since the heat transfer from the rod to the mold is controlled by many unknown parameters, such as the size of the air gap and the emissivities of the materials.

III. SOLIDIFICATION PHENOMENA

During the solidification of brasses in conventional casting processes, a dendritic structure consisting of equiaxed and columnar dendrites is formed. Columnar dendrites are formed from the first solid equiaxed grains at the mold and metal interface, and they grow opposite to the heat flow, developing arms of higher orders. These dendrites can grow as far as to the centerline of the casting. Alternatively, an inner equiaxed zone can be formed in the center of the casting.

During the solidification, different solid phases can also be formed from the melt. The phases formed at different temperatures can be read approximately from the Cu-Zn phase diagram of Figure 3,[24] showing the equilibrium solidification paths for different brasses. All the studied brasses, 85/15, 75/25, 70/30, and 65/35, solidify primarily to the fcc (α) phase. The liquidus temperatures of the alloys can be read from line $x_{\text{Zn}^{\text{L}}}$ and the solidus temperatures of the three first alloys from line $x_{\text{Zn}^{\text{fcc}}}$. Brass 65/35 also undergoes a peritectic reaction at 903 °C. During this, the bcc (β) phase is formed from the fcc and the liquid phase, until the latter one disappears. After that, as the temperature decreases, the fcc phase grows toward the bcc phase, until the latter disappears at about 600 °C. However, at the relatively high cooling rates of this study (50 K/s or higher), these equilibrium solidification paths are no longer valid. This is mainly because of the restricted solute diffusion in the solid, resulting in solute microsegregation and, consequently, in a lower solidus temperature than shown by the diagram. Therefore, nonequilibrium solidification paths had to be calculated in this work, using the MDM model. This procedure is described in Appendix A.

IV. EXPERIMENTAL

The pilot scale trials were undertaken at the Outokumpu Copper Metal Laboratory (Pori, Finland) with a rod upcasting machine. The cast rod was 17 mm in diameter, and the cast materials were oxygen-free copper and four different brasses, 85/15 (copper 85 wt pct and zinc 15 wt pct, respectively), 75/25, 70/30, and 65/35. Experiments were carried out at five different casting speeds, 0.5, 0.7, 0.9, 1.1, and 1.3 m/min, for all the materials. Temperatures of the molten metals in the furnace and the superheats are shown in Table I. Mold temperature measurements were made during all the different castings. The water flow rate was changed from 15 to 25 L/min for copper castings, but held constant at 25 L/min for the brass castings. Furthermore, samples of the cast rod were collected from all castings during the campaign for metallurgical investigation.

Table I. **Important Casting and Mushy Zone Parameters Used in the HTR Model**

Material	Casting Speed (m/min)	Casting Temperature (°C)	Superheat (°C)	Solidus (°C)	Liquidus (°C)	Latent heat (J/g)
Copper	0.5 to 1.3	1150	66	1084	1084	208.7
Brass 85/15	0.5 to 1.3	1120	95	971	1025	191.4
Brass 75/25	0.5 to 1.3	1080	103	905	977	179.2
Brass 70/30	0.5 to 1.3	1020	70	900	950	167.9
Brass 65/35	0.5 to 1.3	980	59	897	921	153.2

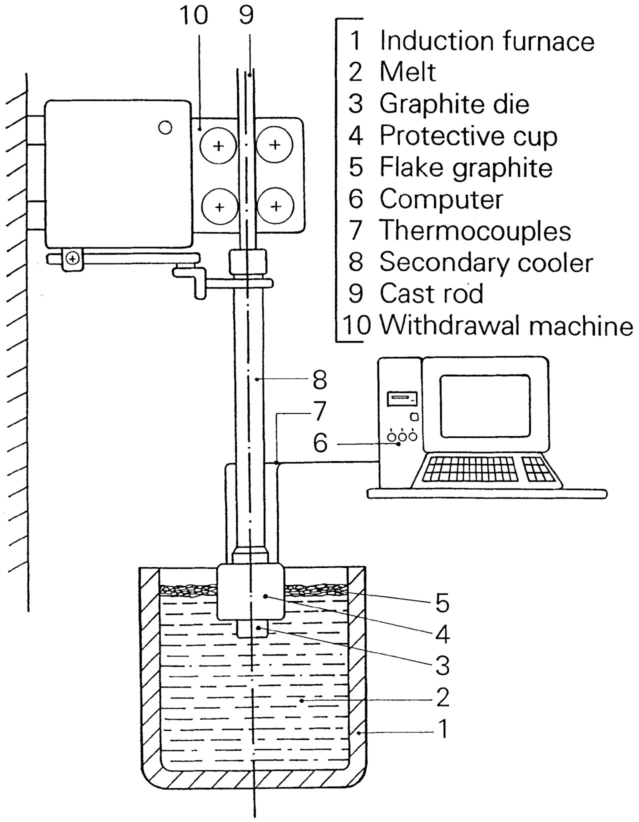

Fig. 4—A schematic layout of the upcasting machine used in the experiments.

A. *Experimental Setup*

The casting device used at the Outokumpu Copper Metal Laboratory consists of a caster, shown in Figure 4, and instrumentation for temperature measurement and the control of water flow rates. The actual caster consisted of a furnace, a cooler, a withdrawal machine, and a coiler. The cooler is located above the furnace. Melting of the charge was carried out in an induction furnace, with a capacity of about 300 kg copper. The cooler consists of the primary (mold) and secondary cooling zones. The primary cooling zone consists of a graphite die, which is partly submerged in molten metal in the furnace. The upper part of the die is surrounded by a water-cooled copper jacket, which causes the molten metal to solidify as it passes through the die. The cooler with the withdrawal machine can be raised or lowered according to the melt level in the furnace, so that the die is always at the same depth in the melt. This also ensures a constant metallostatic pressure during the casting. The rod was pulled by a forward-stop-forward method from the die by tandem pinch rolls and was then guided to the coiler.

B. *Mold Temperature Measurements*

A common method in continuous casting modeling is to calculate the heat flux distribution in the mold by fitting the average amount of heat flux obtained from mold cooling water measurements to experimentally determined heat flux profiles. This method, however, is not accurate enough for studying the solidification in the small scale upcasting mold. Therefore, highly accurate temperature measurements had to be made in order to find the right heat flux profile in the mold.

In order to determine the heat flux distribution in the mold quantitatively, it was necessary to measure the mold wall temperatures. The upcasting mold was instrumented with twelve normal K-type (Ni-Cr) thermocouples, embedded in the water-cooled copper jacket at different locations. Holes for the thermocouples were drilled from the side of the mold and their depth was measured. The thermocouple wires were marked at the specific length and put in place. This was done in order to be sure that the thermocouples were in contact with the copper mold. Consequently, the accuracy of the measurements was governed by the adequacy of the contact between the thermocouple bed and the copper mold. Most of the thermocouples were installed in the bottom part of the mold, in order to detect the start point of the solidification, as well as the formation of the air gap between the solidified shell and the graphite mold. These data were essential for the heat transfer and solidification analysis in this work. Additionally, two thermocouples were installed to measure the surface temperature of the cast rod at the mold exit level. The error limit of the thermocouples used in the experiments was 2.2 °C, and the location of the thermocouples could be defined with an accuracy of 0.5 mm.

The mold of the casting machine consists of a copper mold, a graphite die, an insulation cup, a protective cup, and water channels. The schematic construction of the mold, as well as the temperature measuring points are shown in Figure 5. The scale from 0 to 1 at the right edge of the picture is used as the dimension when later presenting the results.

Data on the temperature were obtained automatically from computer using Dasylab software. From the temperature measurements, the average temperatures at the cooling water side were used as the boundary condition for the mold model, and the temperatures measured at the graphite die side were used to adjust the correct heat flux boundary condition at the graphite die boundary.

C. *Metallographic Examination*

Transverse and longitudinal cross sections were cut from the rods in order to investigate grain size and orientation, macro- and microsegregation, fraction of bcc phase, and

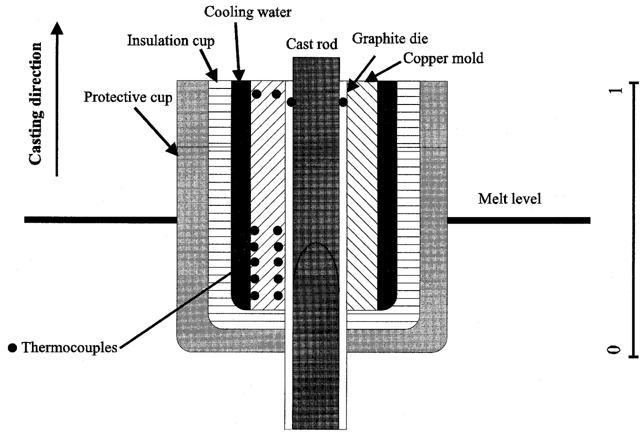

Fig. 5—Structure of the mold showing the location of thermocouples.

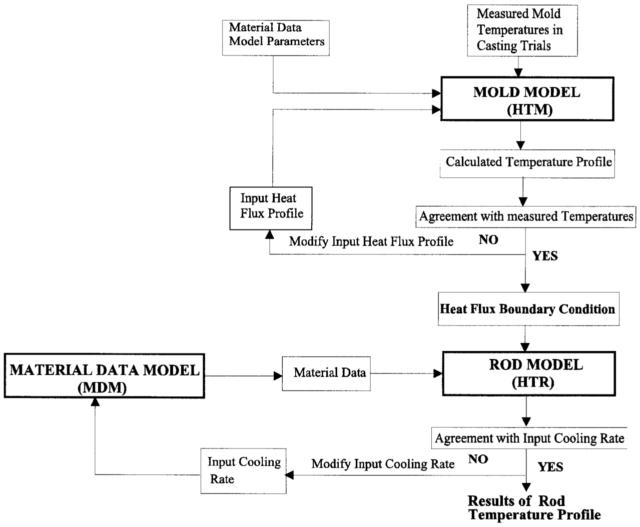

Fig. 6—Flow diagram of the procedure adopted in this study.

secondary dendrite arm spacing. The samples were polished and macroetched at Outokumpu Copper Metal Laboratory to reveal the macrostructure of the samples. Chemical and microstructural analysis was carried out at Outokumpu Research Oy. The microstructure examination was performed with a scanning electron microscope (SEM) and the zinc content of the samples was analyzed with the help of wavelength dispersive spectroscopy (WDS).

V. MATHEMATICAL MODELS

For a better understanding of the heat transfer and solidification procedures in the upcasting mold, mathematical models, HTM and HTR, were constructed to calculate the temperature distribution and the heat fluxes in the mold and cast copper and brass rods. Two separate models were constructed in order to avoid the problem of modeling the air gap formation between the cast rod and the mold. Modeling of the air gap formation would have required simultaneous treatment of heat transfer, solidification, and stress formation. This kind of simulation, however, is numerically very difficult to carry out due to the highly nonlinear mechanical behavior of metals just below the solidification temperature. Additionally, there is a lack of mechanical material data at high temperatures.

The models were produced with the commercial software FIDAP and the details of the solution procedure are presented in the FIDAP theory manua.[25] To obtain reliable results for heat transfer simulations of the HTR model, accurate data on thermophysical properties, such as density, thermal conductivity, and enthalpy, are needed. These data were calculated with the MDM model developed during the study. The MDM model was also used to predict some microstructural properties in the cast rods. The outline of the entire procedure adopted in this study is presented in Figure 6.

A. *Mold Model (HTM)*

A 3-D mathematical model was constructed to simulate the heat transfer in the mold, including the slots machined into the copper mold to facilitate thermocouple installation. The differential equation governing heat conduction in the mold wall under steady-state conditions is given by

$$\frac{\partial\left(k\,\frac{\partial T}{\partial x}\right)}{\partial x}+\frac{\partial\left(k\,\frac{\partial T}{\partial y}\right)}{\partial y}+\frac{\partial\left(k\,\frac{\partial T}{\partial z}\right)}{\partial z}=0 \qquad [5]$$

where k is the thermal conductivity and T is the temperature.

The thermocouple wires were laid along the slots, and the slots consisted of thermocouple wire without a flow of cooling water. Because the thermocouple slots locally increase the mold wall temperature, it was necessary to use a 3-D model, although the basic construction of the mold was axisymmetric. The thermocouple slots near the cooling water side of the mold were not considered in the model, since they were located very close to the cooling water. The measured mold temperatures were converted into heat fluxes at the cast copper or brass rod side of the graphite boundary. The procedure consisted of a manual iterative scheme, in which the heat flux profile at the hot face of the mold was adjusted until the model predicted temperatures agreed with the measured values at the graphite die side of the mold.

The following assumptions were made when constructing the heat flow model.

(1) The mold was considered stationary. Variations in heat flux due to forward-stop-forward motion of the cast wire rod were ignored.
(2) Heat flux across the top and bottom surfaces of the mold and the surfaces within the slot was assumed to be zero.
(3) The temperatures at the cooling water side of the mold were used as boundary conditions, ignoring the disturbance of those thermocouple slots on the heat flow.
(4) Intimate contact was assumed at the interface between the graphite die and the copper mold; *i.e.*, the thermal resistance across the interface was assumed to be zero. In order to solve Eq.[5], the following boundary conditions were used.
(5) Linear temperature interpolation functions on the cooling water side of the mold (T_{CS}) were calculated from the measured temperature points:

$$T_{cs} = T(x) \quad [6]$$

(6) Heat flux boundary condition was applied to the graphite side of the mold:

$$-k \frac{\partial T}{\partial n} = q(x) \quad [7]$$

(7) Heat flux across the top and bottom surfaces of the mold and the surfaces within the slot was assumed to be zero:

$$-k \frac{\partial T}{\partial n} = 0 \quad [8]$$

The material data for copper were calculated with the MDM model. The material data for graphite are the following: thermal conductivity (in W/m K) = 99 - 0.05 (T - 273), specific heat (in J/kg K) = 475 + 1.395T, and density (in kg/m^3) = 1793 (provided by the material supplier).

B. *Rod Model (HTR)*

The other mathematical model, the axisymmetric rod model, was used to simulate the heat transfer and solidification in the cast copper and brass rods. Previously simulated heat fluxes were used in the model as boundary conditions. The equations were solved using the FIDAP 7.5 version.[25] The mass of the rod was moved through this system at the casting speed. The liquid flow of the melt was assumed to be equal to the casting speed; this means that liquid convection in the radial direction was neglected. The governing differential equation was

$$\frac{1}{r}\frac{\partial}{\partial r}\left(rk\frac{\partial T}{\partial r}\right) + \frac{\partial}{\partial x}\left(k\frac{\partial T}{\partial x}\right) - \frac{\partial(\rho c_p V_c T)}{\partial x} + S = 0 \quad [9]$$

where k is the thermal conductivity, T is the temperature, r is the radius of the rod, ρ is the density, C_p is the specific heat, V_c is the casting speed, and S is the source term.

The present simulation involved a calculation problem related to the phase change from liquid to solid copper or brass. In the model, it was possible to include the latent heat either in the source term or the specific heat term. An enthalpy-based approach was provided in the model for evaluating the specific heat (i.e., $S = 0$) for a phase change problem from an enthalpy-temperature curve given in the form

$$c_p = \int H_{\mathrm{tot}} \partial t \quad [10]$$

The following assumptions were made when constructing the heat-flow model.

(1) The liquid flow of the melt was assumed to be equal to the casting speed; this means that liquid convection in the radial direction was neglected.

(2) The flow field was assumed to be constant at any point in the cast copper or brass rod.

(3) Heat flux across the surface against the protective cup was assumed to be zero.

(4) The heat flux boundary condition at the graphite side was set as a boundary condition at the cast rod surface.

(5) The cast rod section was assumed to have a fixed dimension, and consequently, constant density values were used in the calculations.

(6) The heat of the air in the air gap transferred by convection out of the mold was neglected.

(7) The temperature gradient was set to zero at the outlet of the mold, which means that no heat was transferred *via* conduction through the model outlet boundary. Therefore, the model was extrapolated so that the effect of the zero temperature gradient would be meaningless for the calculations in the mold.

In order to solve Eq. [9], the following boundary conditions were used.

(8) The mold wall temperatures were converted, using the mold model, into heat fluxes. They were then used in the brass rod model as boundary conditions:

$$-k \frac{\partial T}{\partial r} = q\ (x) \quad [11]$$

(9) Symmetry around the centerline, as the geometry of the rod is axisymmetric:

$$-k \frac{\partial T}{\partial r} = 0 \quad [12]$$

(10) The temperature of the graphite walls attached to liquid metal was fixed to the casting temperature (T_o = 1253 to 1423 K):

$$T_{\mathrm{wall}} = T_o \quad [13]$$

(11) The heat flux across the surface against the protective cup was assumed to be zero:

$$-k \frac{\partial T}{\partial r} = 0 \quad [14]$$

(12) The temperature of the incoming liquid metal was fixed to the casting temperature (T_o = 1253 to 1423 K):

$$T_{\mathrm{inlet}} = T_o \quad [15]$$

(13) The temperature gradient was set to zero at the outlet of the mold:

$$\frac{\partial T}{\partial x} = 0 \quad [16]$$

The data applied in calculations of the HTR model are shown in Tables I and II.

C. *Model for Material Data and Microstructure*

To obtain reliable results from the heat transfer and solidification simulations, accurate thermophysical data for the material, such as density, thermal conductivity, and enthalpy, are needed. Typically, in metallic alloys, the thermophysical properties of individual solution phases are continuous functions of temperature. In the mushy zone, however, there can be a drastic change in these properties, depending on the intensity of the phase change. Additional changes to the properties are caused by secondary solid phases, *e.g.*, those formed as a result of the peritectic reaction in the mushy zone region.

The alloys in this study (Table I) primarily solidify to the solid fcc structure. In addition, some amount of bcc phase is formed in brasses 70/30 and 65/35, which undergo a peritectic reaction L + fcc → bcc at 903 °C. Note that

Table II. Evaluated Formulas for the Calculation of Enthalpy (H, in J/mol), Density (ρ, in kg/m^3), and Thermal Conductivity (k, in W/m K) in Liquid, Fcc, and Bcc Phases of Cu-Zn System*

Material Property	Temperature Range	Reference
$H^L = x^L_{\mathrm{Cu}}\,(4486 + 43.395T - 2.9644T \ln T + 0.004438T^2) +$ $+ x^L_{\mathrm{Zn}}\,(2594 - 52.287T + 12.0245T \ln T - 0.005627T^2) +$ $+ x^L_{\mathrm{Cu}}\,x^L_{\mathrm{Zn}}\,[-40{,}696 + 4403\,(x^L_{\mathrm{Cu}} - x^L_{\mathrm{Zn}}) + 7818\,(x^L_{\mathrm{Cu}} - x^L_{\mathrm{Zn}})^2]$	$T < 1500$ K	27
$H^{\mathrm{fcc}} = x^{\mathrm{fcc}}_{\mathrm{Cu}}\,(-6727 + 11.528 + 1.8717T \ln T + 0.001111T^2) +$ $+ x^{\mathrm{fcc}}_{\mathrm{Zn}}\,(-230 - 64.741T + 13.6083T \ln T - 0.005769T^2) +$ $+ x^{\mathrm{fcc}}_{\mathrm{Cu}}\,x^{\mathrm{fcc}}_{\mathrm{Zn}}\,[-42{,}804 + 2936\,(x^{\mathrm{fcc}}_{\mathrm{Cu}} - x^{\mathrm{fcc}}_{\mathrm{Zn}}) + 9034\,(x^{\mathrm{fcc}}_{\mathrm{Cu}} - x^{\mathrm{fcc}}_{\mathrm{Zn}})^2]$	$T < 1500$ K	27
$H^{\mathrm{bcc}} = x^{\mathrm{bcc}}_{\mathrm{Cu}}\,(-2710 + 11.528T + 1.8717T \ln T + 0.001111T^2) +$ $+ x^{\mathrm{bcc}}_{\mathrm{Zn}}\,(-313 - 64.741T + 13.6083T \ln T - 0.005769T^2) +$ $+ x^{\mathrm{bcc}}_{\mathrm{Cu}}\,x^{\mathrm{bcc}}_{\mathrm{Zn}}\,[-51{,}596 + 7562\,(x^{\mathrm{bcc}}_{\mathrm{Cu}} - x^{\mathrm{bcc}}_{\mathrm{Zn}}) + 30{,}744\,(x^{\mathrm{bcc}}_{\mathrm{Cu}} - x^{\mathrm{bcc}}_{\mathrm{Zn}})^2]$	$T < 1500$ K	27
$\rho^L = x^L_{\mathrm{Cu}}\,(9086 - 0.801T) + x^L_{\mathrm{Zn}}\,(7336 - 1.1T) + x^L_{\mathrm{Cu}}\,x^L_{\mathrm{Zn}}\,(1143 + 0.268T)$		28, 29
$\rho^{\mathrm{fcc}} = x^{\mathrm{fcc}}_{\mathrm{Cu}}\,(9097 - 0.521T) + x^{\mathrm{fcc}}_{\mathrm{Zn}}\,(7349 - 0.715T) +$ $+ x^{\mathrm{fcc}}_{\mathrm{Cu}}\,x^{\mathrm{fcc}}_{\mathrm{Zn}}\,[(581 + 0.193T) + (-689 + 0.476T) \cdot 10^{-5x^{\mathrm{fcc}}_{\mathrm{Zn}}}]$		29 through 33
$\rho^{\mathrm{bcc}} = x^{\mathrm{bcc}}_{\mathrm{Cu}}\,(8268 - 0.109T) + x^{\mathrm{bcc}}_{\mathrm{Zn}}\,(8765 - 1.186T)$		30, 31
$k^L = x^L_{\mathrm{Cu}}\,(127.2 + 0.0267T) + x^L_{\mathrm{Zn}}\,(9.3 + 0.058T)$ $+ x^L_{\mathrm{Cu}}\,x^L_{\mathrm{Zn}}\,[(-175 - 0.049T) + (-676 - 0.54T) \cdot 10^{-4x^L_{\mathrm{Zn}}}]$		28
$k^{\mathrm{fcc}} = x^{\mathrm{fcc}}_{\mathrm{Cu}}\,(399.2 + 0.1605T - 0.02935T \ln T) + x^{\mathrm{fcc}}_{\mathrm{Zn}}\,(125.7 - 0.0437T) +$ $+ x^{\mathrm{fcc}}_{\mathrm{Cu}}\,x^{\mathrm{fcc}}_{\mathrm{Zn}}\,[-378 - 2887 \cdot 10^{-2.5x^{\mathrm{fcc}}_{\mathrm{Zn}}}]$		29, 34
$k^{\mathrm{bcc}} \approx k^{\mathrm{fcc}}$		

*By dividing the enthalpy functions with $x^{\mathrm{nom}}_{\mathrm{Cu}}\,M_{\mathrm{Cu}} + x^{\mathrm{nom}}_{\mathrm{Zn}}\,M_{\mathrm{Zn}}$, H in J/g is obtained (here, x^{nom}_i is the nominal composition and M_i is the atomic weight of component i). References on the right refer to the original data exploited in the evaluation process.

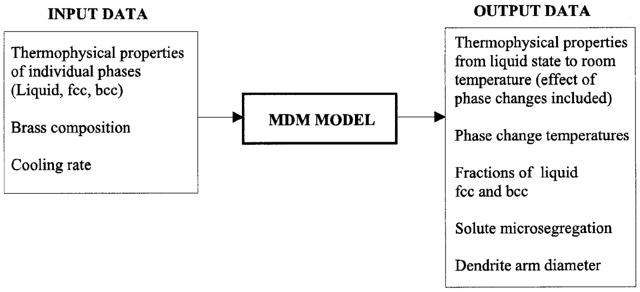

Fig. 7—Schematic presentation of the MDM model

according to the experimental Cu-Zn phase diagram of Figure 3, no high-temperature bcc phase is formed in brass 70/30, but at the finite cooling rates of real processes, this is possible. In order to calculate the thermophysical properties of the mushy zone affected by the peritectic reaction, one should know the properties of the individual phases, L, fcc, and bcc, and the fractions of these phases as a function of temperature.

Using the MDM model, special functions were developed to calculate thermophysical properties, *i.e.*, enthalpy, density, and thermal conductivity, for Cu-Zn alloys in the single phase regions of liquid, fcc, and bcc and in the phase change regions. In the latter case, one has to know the phase fractions as a function of temperature. These were calculated in a conventional way,[26] using mass balance equations of phase interfaces (fcc/L, bcc/L, fcc/bcc) and Fick's second law of solute diffusion in a solid (fcc and bcc) on a scale of one volume element set on the side of a dendrite arm (Appendix A). The schematic presentation of the MDM model is shown in Figure 7.

1. *Thermophysical property functions of liquid, fcc, and bcc phases*

Thermophysical material data for the liquid, fcc, and bcc phases of Cu-Zn alloys are given in References 27 through 34. In the MDM model, these experimental or assessed data were fitted to the form of the equation

$$P^{\phi} = x^{\phi}_{\mathrm{Cu}}\;{}^0P^{\phi}_{\mathrm{Cu}} + x^{\phi}_{\mathrm{Zn}}\;{}^0P^{\phi}_{\mathrm{Zn}} + x^{\phi}_{\mathrm{Cu}}x^{\phi}_{\mathrm{Zn}}\;P^{\phi}_{\mathrm{CuZn}} \qquad [17]$$

Here, property P stands for enthalpy H, density ρ, or thermal conductivity k; phase ϕ stands for liquid, fcc, and bcc; ${}^0P_{\mathrm{Cu}}{}^{\phi}$ and ${}^0P_{\mathrm{Zn}}{}^{\phi}$ are the properties of pure Cu and Zn; $P^{\mathrm{CuZn}\phi}$ is a parameter describing the deviation from the ideal behavior of the Cu-Zn mixture; and $X_{\mathrm{Cu}}{}^{\phi}$ and $X_{\mathrm{Zn}}{}^{\phi}$ are the mole fractions of Cu and Zn. Parameters ${}^0P_{\mathrm{Cu}}{}^{\phi}$ and ${}^0P_{\mathrm{Zn}}{}^{\phi}$ are functions of temperature, and parameter $P_{\mathrm{CuZn}}{}^{\phi}$ can be a function of temperature and/or composition. The advantage of using these functions is that the changes in the property values caused by the compositional changes during solidification (*i.e.*, microsegregation and solute enrichment in the liquid) can be taken into account. The developed functions for enthalpy, density, and thermal conductivity in the liquid, fcc, and bcc phases are shown in Table II.

In the case of enthalpy, the functions were calculated from the substitutional solution Gibbs energy data of the Cu-Zn system by Kowalski and Spencer[27] as

$$H^{\phi} = G^{\phi} - \left(\frac{\partial G^{\phi}}{\partial T}\right)_P \qquad [18]$$

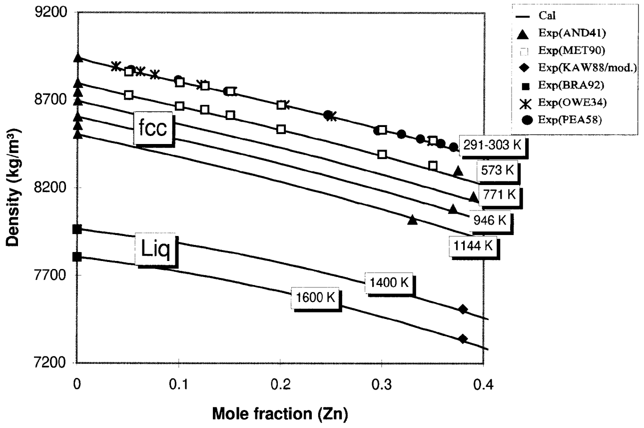

Fig. 8—Experimental[28–33] and calculated densities in the liquid and the fcc phase of brass.

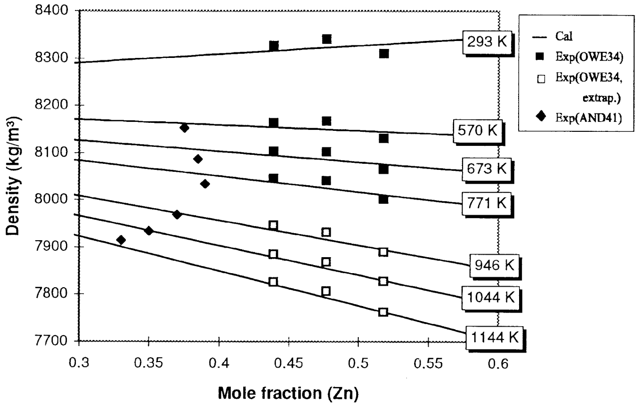

Fig. 9—Experimental[30,31] and calculated density in the bcc phase of brass.

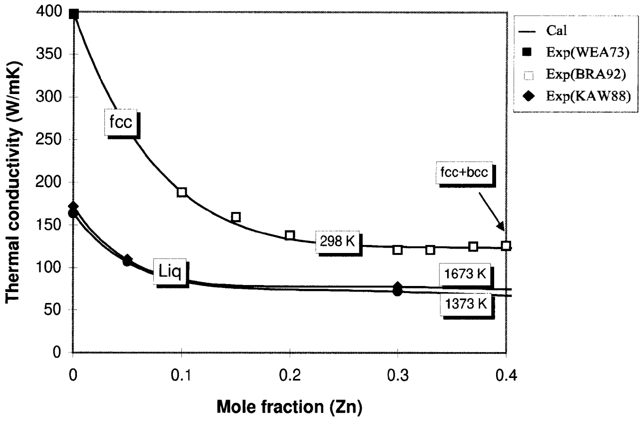

Fig. 10—Experimental[28,29,34] and calculated thermal conductivities in the liquid and the fcc phase of brass.

where G^ϕ is the molar Gibbs energy of liquid, fcc, and bcc phases given as

$$\begin{aligned} G^\phi = {} & x^\phi_{Cu}\,({}^0G^\phi_{Cu} - H^{SER}_{Cu}) + x^\phi_{Zn}\,({}^0G^\phi_{Zn} - H^{SER}_{Zn}) \\ & + x^\phi_{Cu}\,RT\ln x^\phi_{Cu} + x^\phi_{Zn}\,RT\ln x^\phi_{Zn} + \\ & + x^\phi_{Cu}x^\phi_{Zn}\,[{}^0L^\phi_{CuZn} + {}^1L^\phi_{CuZn}\,(x^\phi_{Cu} - x^\phi_{Zn}) \\ & + {}^2L^\phi_{CuZn}\,(x^\phi_{Cu} - x^\phi_{Zn})^2] \end{aligned} \qquad [19]$$

In Eq. [19], ${}^0G_{Cu}{}^\phi$-$H_{Cu}{}^{SER}$ and ${}^0G_{Zn}{}^\phi$-$H_{Zn}{}^{SER}$ describe the Gibbs energies of pure Cu and Zn in phase ϕ relative to a special reference state SER,[35] and ${}^nL_{CuZn}{}^\phi$ ($n = 0, 1, 2$) are parameters describing the nth order interactions between Cu and Zn in phase ϕ. When applying Eqs. [18] and [19], the temperature dependency of the enthalpy data was simplified to obtain simpler enthalpy functions in the temperature range 298 to 1500 K. These simplified functions given in Table II correlate well with the original experimental mixing enthalpy data.[27] In the case of density and thermal conductivity, the functions (Table II) were formed using the experimental data of References 28 through 34. As a result, a good correlation was obtained between the optimized functions and the original measurements, as shown in Figures 8 through 10. In the case of the liquid density data, one should notice that the two data points of Figure 8 at Zn content 38 wt pct represent the mean values of the reported experimental data points[28] and the data points calculated from Eq. [17] assuming $\rho_{CuZn}{}^L$ equal to zero (ideal mixing behavior). This approximation was adopted due to the fact that using the reported experimental data only would have resulted in solidification expansion in brasses 70/30 and 65/35 (liquid too dense with respect to solid) not reported in the literature.[33] Nevertheless, careful density measurements of liquid brasses are necessary before one can get a reliable prediction for the shrinking behavior of solidifying brasses. In the case of the bcc density data, one should notice that the function of Eq. [17] is described by means of terms ${}^0\rho_{Cu}{}^{bcc}$ and ${}^0\rho_{Zn}{}^{bcc}$ only. This was done for convenience, in spite of the fact that bcc is not a stable phase for pure Cu and pure Zn. Finally, due to the lack of thermal conductivity data for the bcc phase, the data were assumed to be equal to the data of the fcc phase. This assumption can be justified on the basis of the k^{fcc} data of Figure 10 at 298 K, showing no drastic change when moving from the fcc to the fcc + bcc region.

2. *Thermophysical property functions of phase change region*

Provided that, in the phase change regions (*e.g.*, the mushy zone), the phase fractions are known as a function of temperature, one is able to estimate the thermophysical properties in these regions. In the phase change regions, enthalpy H, density ρ, and thermal conductivity k can be described with equations

$$H = f^L\,H^L + f^{fcc}\,H^{fcc} + f^{bcc}\,H^{bcc} \qquad [20]$$

$$\rho = 1/\left[\frac{f^L}{\rho^L} + \frac{f^{fcc}}{\rho^{fcc}} + \frac{f^{bcc}}{\rho^{bcc}}\right] \qquad [21]$$

$$k = f^{fcc}\,k^{fcc} + f^{bcc}\,k^{bcc} + (1 + A_{mix})f^Lk^L \qquad [22]$$

where f^ϕ is the fraction of phase ϕ (ϕ = L, fcc, bcc, $f^L + f^{fcc} + f^{bcc} = 1$), and H^ϕ, ρ^ϕ, and k^ϕ are the molar enthalpy, the density, and the thermal conductivity of that phase, respectively. Functions based on Eq. [17] for H^ϕ, ρ^ϕ, and k^ϕ have been given in Table II. In the case of thermal conductivity in Eq. [22], A_{mix} is a liquid-convection parameter where value zero means no convection in the liquid. In the upcasting process of this study, the convection was assumed to be negligible, and hence, $A_{mix} = 0$. These Eqs. [20] through [22] of the phase change region are, of course, also valid in single phase regions L, fcc, and bcc. For example, above the liquidus temperature, $f^L = 1$ and $P = P^L$, and below the solidus temperature, $f^L = 0$ and $P = f^{fcc}P^{fcc}$

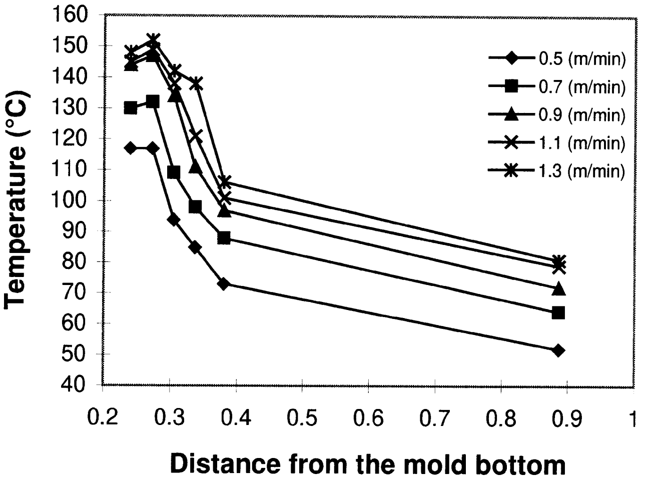

Fig. 11—Temperature profiles at the graphite die side of the mold for copper.

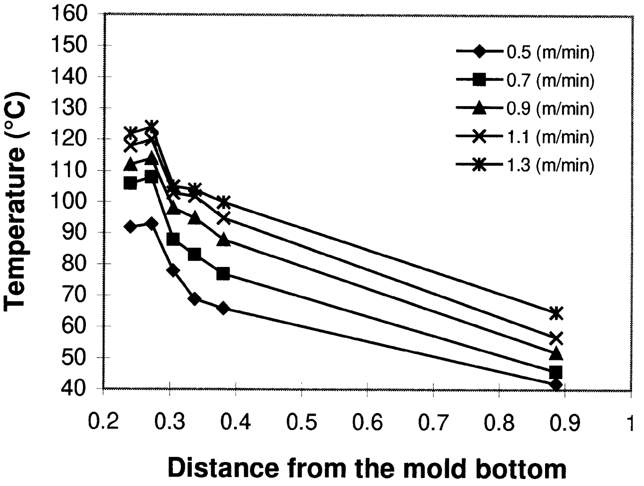

Fig. 12—Temperature profiles at the graphite die side of the mold for brass 65/35.

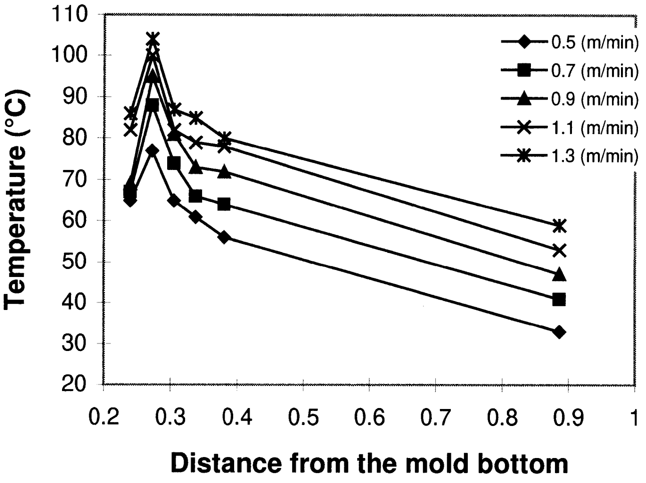

Fig. 13—Temperature profiles at the cooling water side of the mold for copper.

$+ f^{bcc} P^{bcc}$, which reduces to $P = P^{fcc}$ if no bcc phase was formed ($P = \rho, k, H$). Finally, it should be remembered that, in the mushy zone, not only the changing phase fractions but also the changing phase compositions, $x_{Zn}{}^{\phi}$ and $x_{Cu}{}^{\phi} = 1 - x_{Zn}{}^{\phi}$ (ϕ = L, fcc, bcc), will affect the thermophysical properties of Eqs. [20] through [22]. In the case of composition, the effect is due to influence on the thermophysical properties of the phases *via* Eq. [17]. In the case of liquid, the interfacial liquid compositions can be applied directly (uniform composition profiles assumed in liquid). However, in the case of fcc and bcc phases, one must apply the average compositions calculated from the concentration profiles, instead of the interfacial compositions $x_{Zn}{}^{\phi}$ and $x_{Cu}{}^{\phi}$ in Eq. [17].

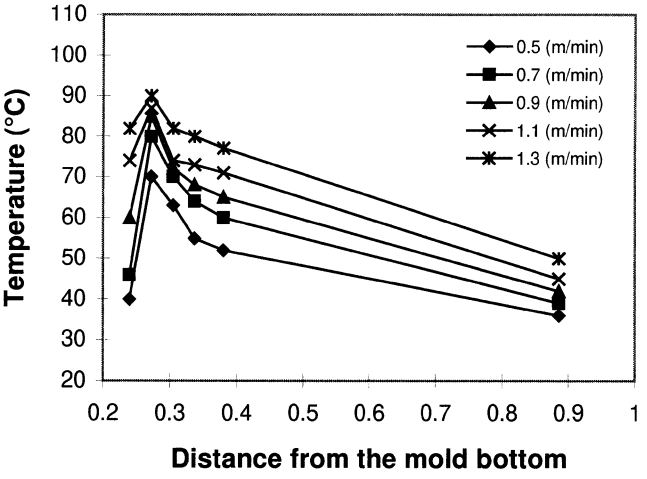

Fig. 14—Temperature profiles at the cooling water side of the mold for brass 65/35.

VI. RESULTS

In this work, temperature measurements, metallographic analysis, and mathematical modeling have been applied to establish a basic knowledge of heat transfer and solidification in the upcasting mold for copper and brasses. The experimental part of the results is presented in the following three sections: A, B, and C, showing temperature measurements of the mold, temperature measurements of the cooling water, and metallographic analysis of the cast rod samples. The theoretical part of the results was produced with the mathematical models in Section V and is presented here in Section D. This section also presents some comparisons between measured and calculated results, giving an estimation of the validity of the models.

A. *Mold Temperature Measurements*

Temperature measurements were made in the copper jacket of the mold for a fixed water flow rate of 25 L/min. From these measurements, the average temperatures were used in the calculations of the HTM model. Figures 11 through 14 show the average temperature profiles along the length of the mold for various casting speeds at the graphite die side and the cooling water side of the mold.

The axial temperature profiles at the graphite die side and the cooling water side of the copper mold give a qualitative insight into the heat flow in the mold. In the casting direction, the temperature of the mold wall is not uniform, reflecting a considerable variation in the heat transfer rate from the copper rod to the mold wall. The temperature

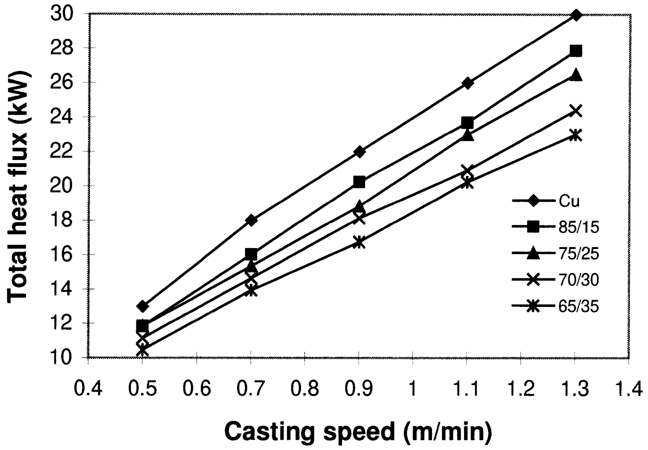

Fig. 15—Total heat flux from the rod into the cooling water for different castings.

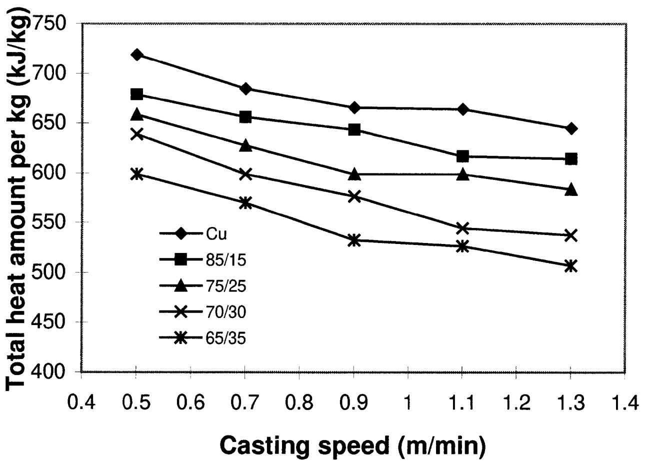

Fig. 16—Total heat extracted per kilogram from the rod for different castings.

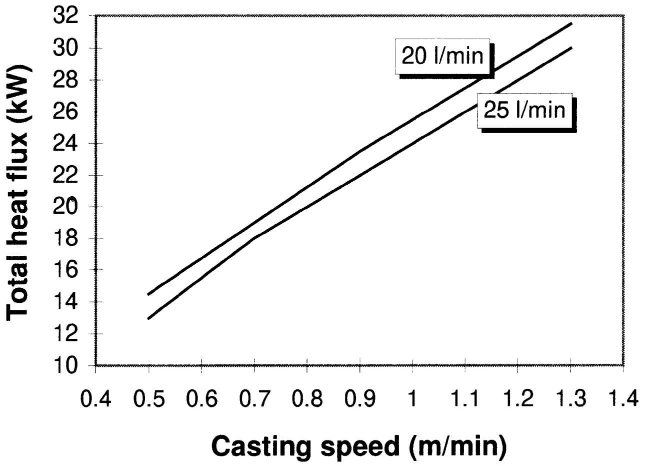

Fig. 17—Total heat flux from the copper rod into the cooling water with water velocities of 20 and 25 L/min.

reaches a maximum value close to the first contact point between the copper mold and the graphite die. After that, it drops due to a combination of air gap formation and thickening of the solid shell.

The influence of casting speed on the cold side and the hot side temperature profiles of the mold can be seen in Figure 11 and 13 for copper and in Figure 12 and 14 for brass 65/35. Increasing the casting speed shifts up the temperature profiles quite uniformly, so that the form of the profiles remains essentially the same. This is valid for all the cast materials. In each profile, one can find a peak of maximum temperature located slightly above the first contact point between the copper mold and the graphite die and a minimum temperature located at the mold exit level. For example, increasing the casting speed from 0.5 to 1.3 m/min for copper raises the hot side temperature peak by 36 °C (from 117 °C to 153 °C) and the minimum temperature by 32 °C (from 51 °C to 83 °C). In all of the casting examples, the maximum temperature values varied between 95 °C and 153 °C and the minimum temperature values varied between 40 °C and 83 °C.

With increasing zinc content of the alloy, the temperature profiles of the mold were lowered. This can be seen in Figures 11 through 14, showing the higher located temperature profiles for copper and the lower located temperature profiles for brass 65/35. In the other brasses, the temperature profiles were located between these two extremes. The individual effect of zinc, however, could not be determined accurately due to the different casting temperatures of the cast materials.

B. *Cooling Water Measurements*

The temperatures of the outgoing cooling water were measured for brasses using a fixed water flow rate of 25 L/min. The water flow rate was changed from 20 to 25 L/min for copper castings only. The cooling water circulation consists of a primary (mold) and a secondary cooling part (Figure 4). Consequently, the results not only show the efficiency of the mold, but also that of the secondary cooling unit located directly above the mold. Figure 15 shows the influence of the casting speed on the total heat flux (in kilowatts) extracted from the cast rod for all the cast materials. In all cases, increasing the casting speed raises the total heat flux transferred from the cast rod into the cooling water. For example, increasing the casting speed from 0.5 to 1.3 m/min for copper raises the transferred heat flux from 12.5 to 29 kW. The influence of casting speed on the total heat change per unit weight (in kJ/kg) is shown in Figure 16. In all cases, increasing the casting speed decreases the total heat change per kilogram.

Figure 17 shows the comparison of heat extraction from copper with cooling water velocities of 20 and 25 L/min. It can be seen that with lower cooling water velocity, the heat extraction is higher. This is indicated upon boiling of the cooling water. The nucleation of bubbles needs a lot of energy, and so the heat transfer is increased when boiling of cooling water takes place. Experiments with 15 L/min were also performed, but a steady-state situation was never achieved, as the cooling water temperature increased by over 30 °C and the cooling water flow rate was increased for safety reasons.

C. *Metallographic Analysis*

Transverse and longitudinal slices were cut from the rod samples in order to examine grain sizes and orientations, secondary dendrite arm spacings, phase distribution, and

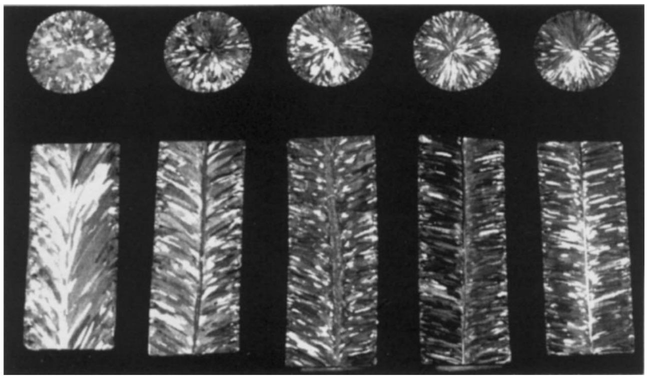

Fig. 18—Transverse and longitudinal cross sections of the copper rod with different casting speeds.

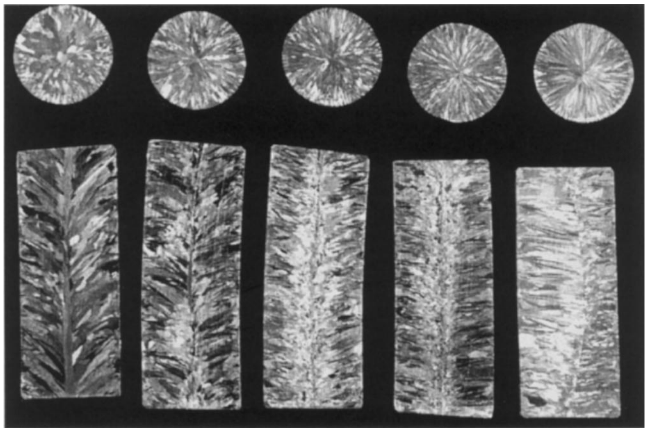

Fig. 19—Transverse and longitudinal cross sections of the brass 85/15 rod with different casting speeds.

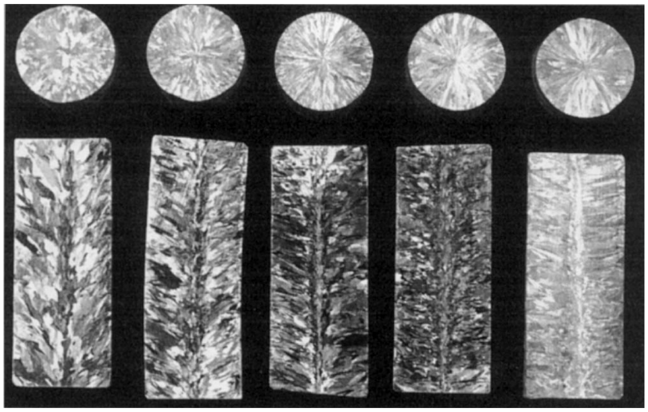

Fig. 20—Transverse and longitudinal cross sections of the brass 75/25 rod with different casting speeds.

macro-and microsegregation. The samples were polished and macroetched to reveal the macrostructure of the samples. The microstructure of the samples was studied with an SEM, and the macro- and microsegregation of zinc in the samples was analyzed with WDS.

1. *Macrostructure*

Each sample was cut vertically and horizontally and was metallographically prepared. The macrostructure resulting from solidification could be clearly revealed by macroetching the copper and the brass rods. Figures 18 through 22 show the sample macrostructure of the transverse and the longitudinal transverse and longitudinal cross sections at different casting speeds. The outer chill zone and the columnar zone can be clearly seen in all samples. With increasing casting speed, the orientation of the columnar grains is changed from an axial/radial direction to a more radial direction. As the columnar grains tend to grow toward the main heat flux, the direction of that flux can also be revealed from these samples. The average grain size becomes smaller with the increasing casting speed, as the grains have a shorter time to grow at high temperatures just below the solidus temperature.

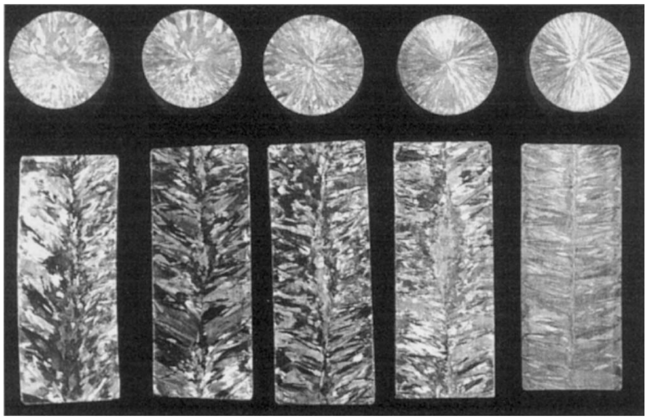

Fig. 21—Transverse and longitudinal cross sections of the brass 70/30 rod with different casting speeds.

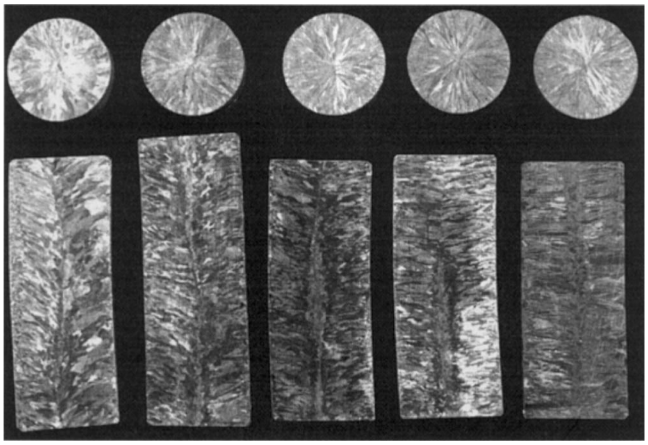

Fig. 22—Transverse and longitudinal cross sections of the brass 65/35 rod with different casting speeds.

2. *Microstructure*

The microstructure of the samples was also analyzed. Figure 23 shows the microstructure of brass 65/35. This structure could only be revealed for brass 65/35. The dendrites in Figure 23(a) are from the centerline of the longitudinal cross section. After revealing the dendritic structure in a specimen, quantitative determinations of some microstructural dimensions of dendrites are usually made. In most studies, attention has been focused on measuring the spacings of secondary dendrite arms grown from the primary dendrite trunks. The secondary dendrite arms between the centerline and the surface of brass 65/35 can be clearly seen in Figure 23(b).

Figures 24 and 25 show the phase distribution in the cast

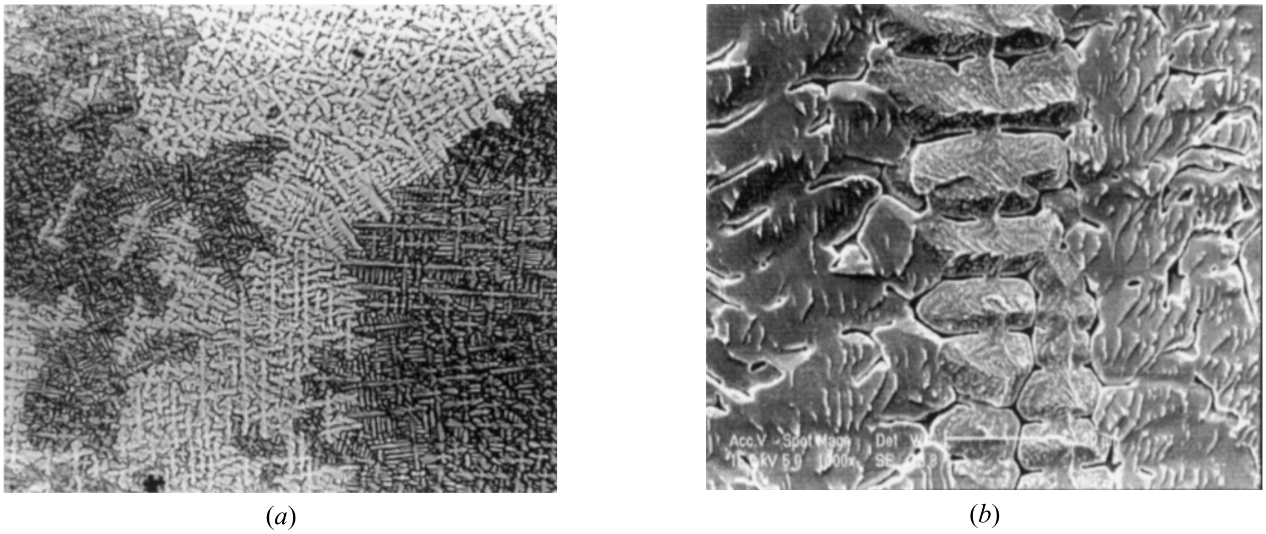

(*a*) (*b*)

Fig. 23—(*a*) Dendrites at the centerline of brass 65/35 (magnification 150 times) (*b*) with a magnification of some dendrites between the centerline and the surface of the cast rod.

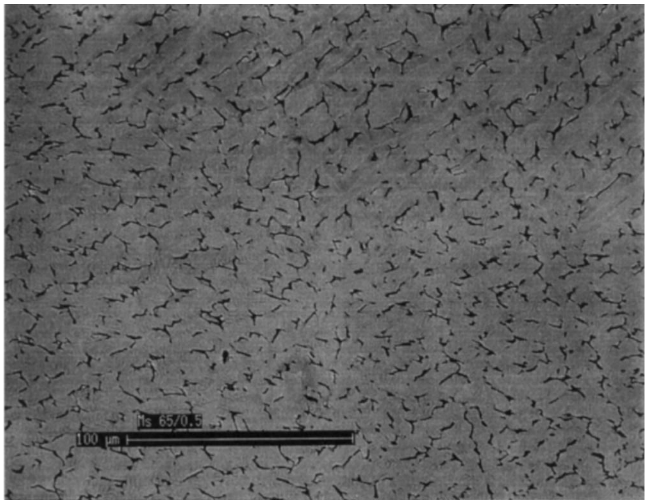

Fig. 24—Microstructure of brass 65/35 showing some bcc phase (dark areas) in the fcc matrix (light area).

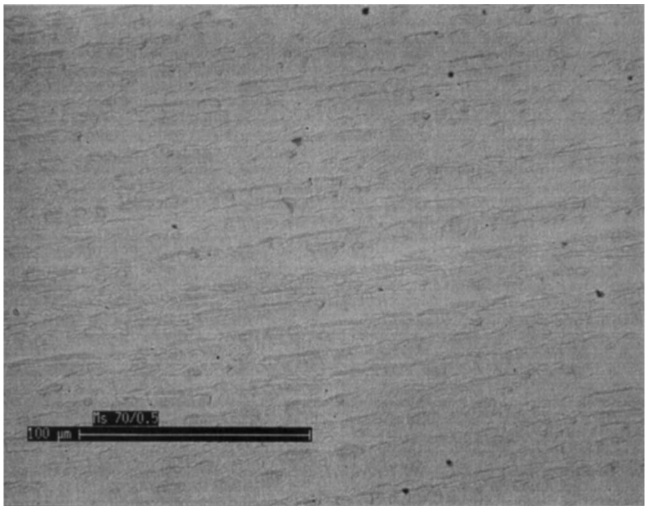

Fig. 25—Microstructure of brass 70/30 showing a pure fcc structure with no bcc phase.

rod samples of brasses 65/35 and 70/30. The bcc phase is shown as dark areas and the fcc phase as light areas. As can be seen, brass 65/35 contains some bcc phase in the fcc matrix, whereas brass 70/30 has a pure fcc structure with no bcc phase. These observations are supported by the comparison of measured and calculated bcc fractions shown in Section D.

3. *Macro- and microsegregation*

Based on the analysis with WDS, no macrosegregation of zinc was observed in the cast brass samples. This may originate from insignificant liquid flows being incapable of transporting solute atoms between the dendrites. The WDS measurement revealed that zinc microsegregated in the scale of dendrites. Some microsegregations of zinc have been compared with calculated values in Section D.

D. *Mathematical Models*

For a further understanding of the heat transfer and the solidification phenomena in the upcasting mold, three mathematical models, HTM, HTR, and MDM (Section V) were applied.

1. *Mold model (HTM)*

The comparison of the axial temperature profiles between the graphite die side and cooling water side of the mold show that there are differences in the temperatures along the length of the copper mold (Figures 11 through 14). The observed differences cannot be rationalized without a quantitative description of the heat transfer in the mold. Thus, the HTM model of the mold was constructed to characterize the heat transfer rates from the measured mold temperature data.

Figures 26 through 30 show the heat flux profiles calculated using the 3-D HTM model. As can be seen, the interfacial heat flux during solidification has a maximum peak value varying from 8000 to 14000 kW/m^2 (close to the first contact point between the copper mold and the graphite die) and a minimum value varying from 800 to 2200 kW/m^2 (at the mold exit level), depending on the casting speed and the cast material. Increasing the casting speed

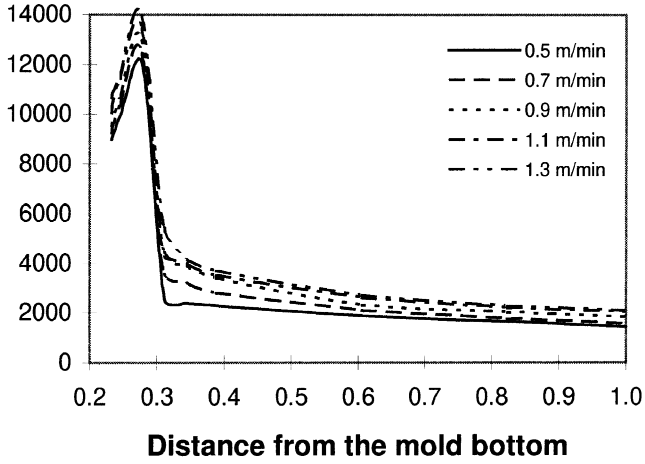

Fig. 26—Calculated heat flux profiles at the graphite interface for copper.

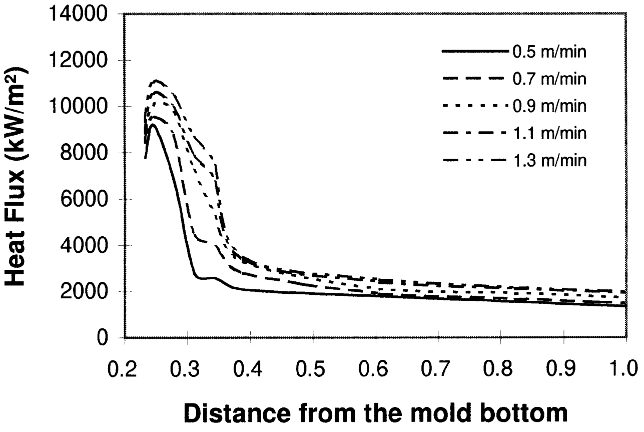

Fig. 27—Calculated heat flux profiles at the graphite interface for brass 85/15.

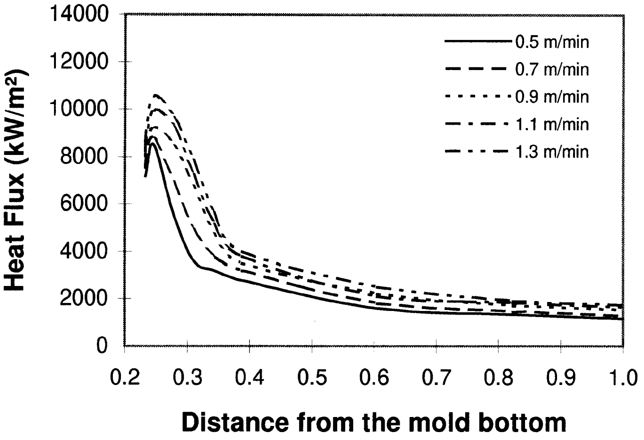

Fig. 28—Calculated heat flux profiles at the graphite interface for brass 75/25.

shifts up the heat flux profile, retaining the essential form of the profile. This is valid for all the cast materials. The air gap formation starts at approximately the same place with all cast materials. An increase in the casting speed shifts the location of the air gap formation slightly upward.

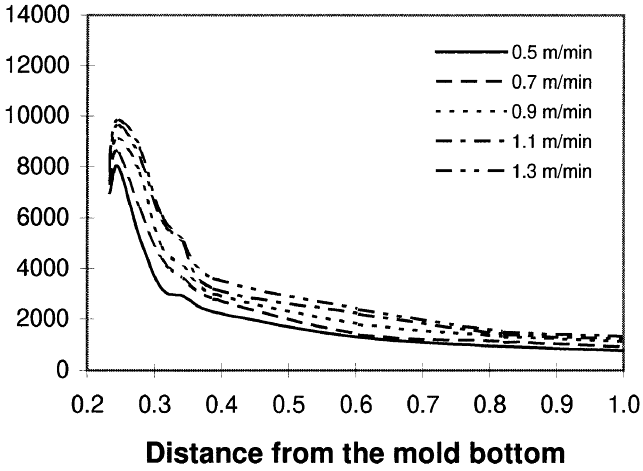

Fig. 29—Calculated heat flux profiles at the graphite interface for brass 70/30.

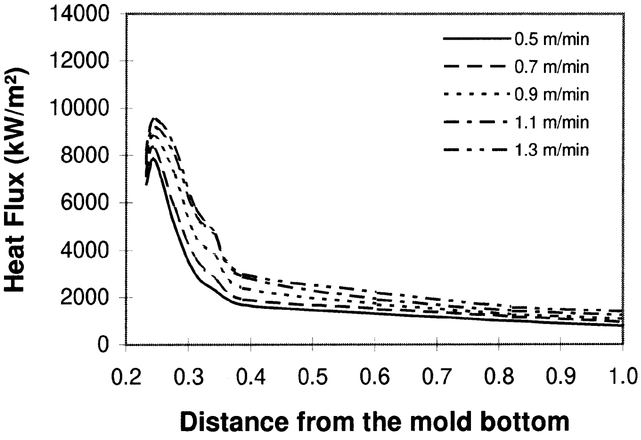

Fig. 30—Calculated heat flux profiles at the graphite interface for brass 65/35.

The total heat flux is higher for copper than for the brasses, but the difference can partly be explained by the different casting temperatures of the materials. The maximum peak value of heat flux decreases with increasing zinc content in the following way: 14,000 kW/m^2 for copper, 11,000 kW/m^2 for brass 85/15, 10,500 kW/m^2 for brass 75/25, 9900 kW/m^2 for brass 70/30, and 9600 for brass 65/35. The minimum value (at the mold exit level) of heat flux decreases with increasing zinc content in the following way: 1450 kW/m^2 for copper, 1350 kW/m^2 for brass 85/15, 1150 kW/m^2 for brass 75/25, 850 kW/m^2 for brass 70/30, and 800 for brass 65/35.

2. *Rod model (HTR)*

The HTR model was constructed to simulate the heat transfer and solidification phenomena in the cast rod. The previously calculated heat fluxes (HTM model) were used in the HTR model as boundary conditions and the thermophysical data needed in the calculations were simulated with the MDM model.

Figure 31 shows the height of the solidus front from the first contact point between the copper mold and graphite die for copper, and the brasses, at different casting speeds. As can be seen, increasing the casting speed increases the distance quite linearly.

Figures 32 through 34 show the shape and the position of the solidus front (S) and the liquidus front (L) at different casting speeds for copper, brass 85/15, and brass 65/35,

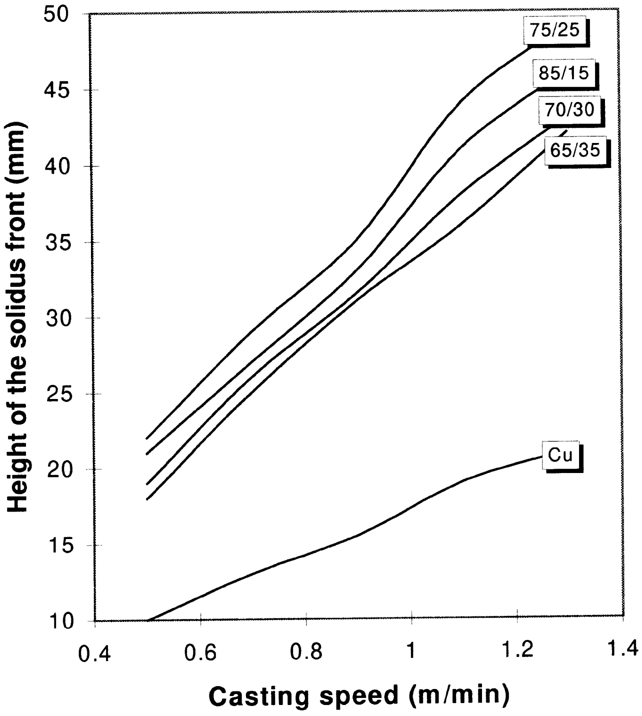

Fig. 31—Height of the solidus front for copper and brasses 85/15, 75/25, 70/30, and 65/35 as a function of casting speed.

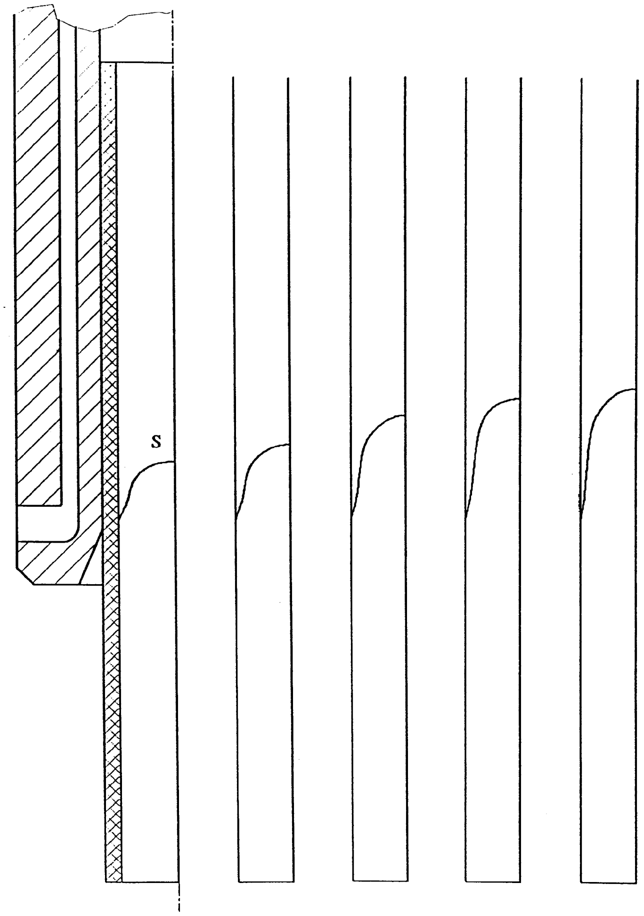

Fig. 32—Shape and position of the solidification front (S) for copper at different casting speeds.

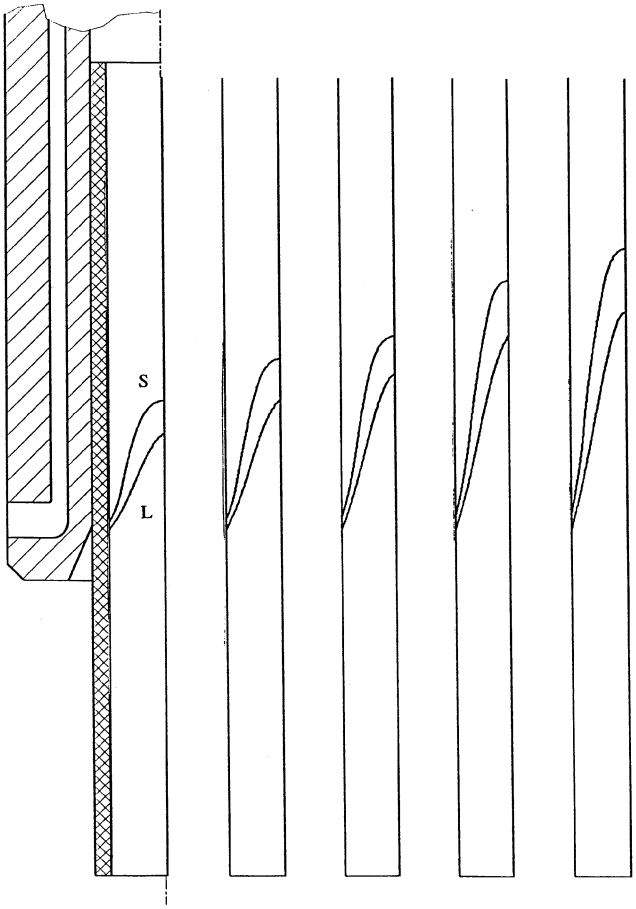

Fig. 33—Shape and position of the solidus front (S) and the liquidus front (L) for brass 85/15 at different casting speeds.

respectively. Due to the axisymmetric nature of the rod samples, only half of the rod, from the rod surface to its center, is shown. The mold has been added to these figures to clearly illustrate the position of the mushy zone, *i.e.*, the zone where the solidification takes place. Increasing the casting speed shifts up both the solidus and liquidus fronts quite linearly. It also enlarges the mushy zone of the brasses. Generally, the higher the casting speed, the later the rod will be fully solidified.

Figures 35 through 39 show the center and the surface temperatures along the length of the cooler for copper and the brasses with two casting speeds, 0.5 and 1.3 m/min. The solidus and the liquidus temperatures are marked in the figures, with horizontal dashed lines determining the mushy zone area for each case. As can been seen, the solidification always begins at approximately the same place, at a distance of 0.2 from the mold bottom, regardless of the cast material or the casting speed. The solid shell forms very quickly, while the centerline remains in the liquid state for some time. After the nucleation of the first solid crystals at the mold wall, the crystals start to grow inward. At the beginning of the solidification, a lot of latent heat is released due to the large amount of liquid phase compared to solid phase. The cast rod center temperature decreases very slowly until the end of the solidification, when only a little of the latent heat is unreleased, and the temperature drop is much faster. This can be seen in Figures 35 through 39. It is also quite evident that a higher casting speed in-

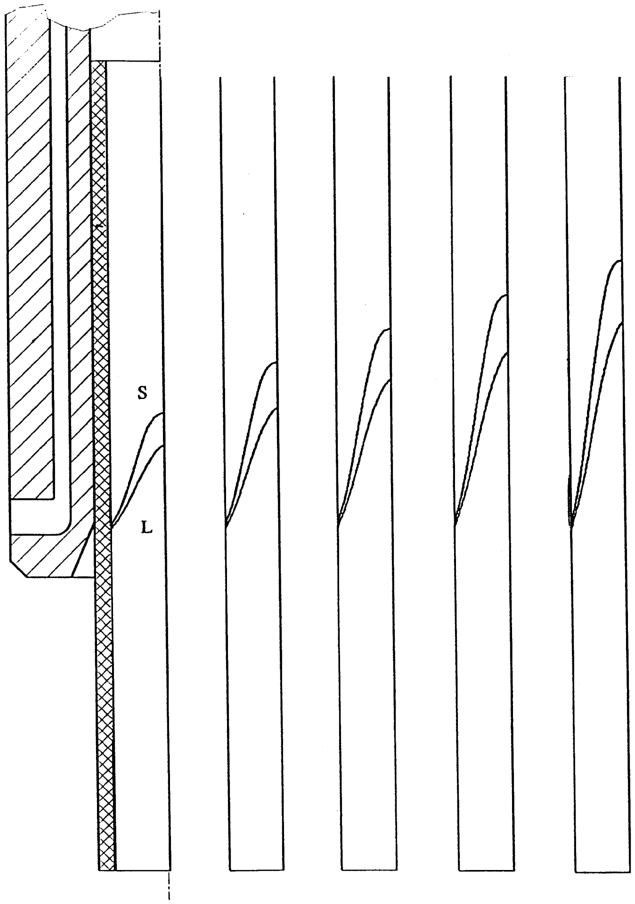

Fig. 34—Shape and position of the solidus front (S) and the liquidus front (L) for brass 65/35 at different casting speeds.

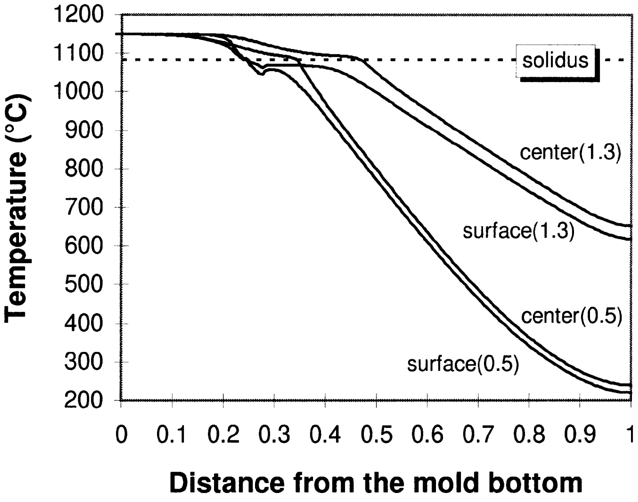

Fig. 35—Center and surface temperatures along the length of the mold for copper at casting speeds of 0.5 and 1.3 m/min.

creases the difference between the surface and center temperatures at the mold exit level for all the cast materials.

The solidus temperatures of brasses 85/15 and 75/25 are clearly lower than the equilibrium solidus temperatures (Figure 3). This is due to the relatively high cooling rates in this study (50 K/s or higher), where equilibrium solidification paths are no longer valid. This is mainly due to restricted solute diffusion in the solid fcc phase, resulting in solute microsegregation and, consequently, a lower solidus temperature than is shown by the diagram. In brasses

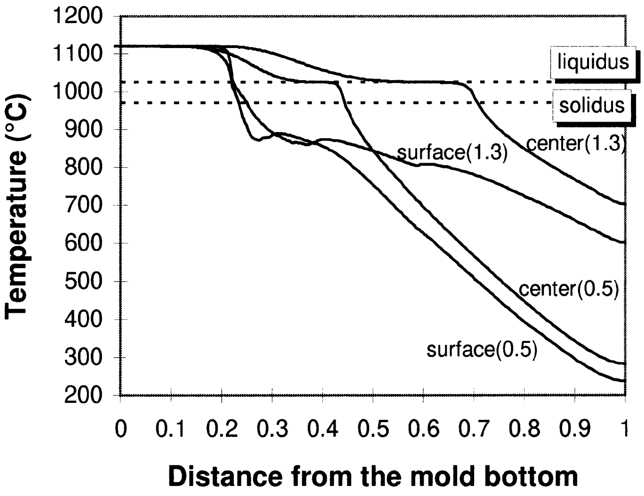

Fig. 36—Center and surface temperatures along the length of the mold for brass 85/15 at casting speeds of 0.5 and 1.3 m/min.

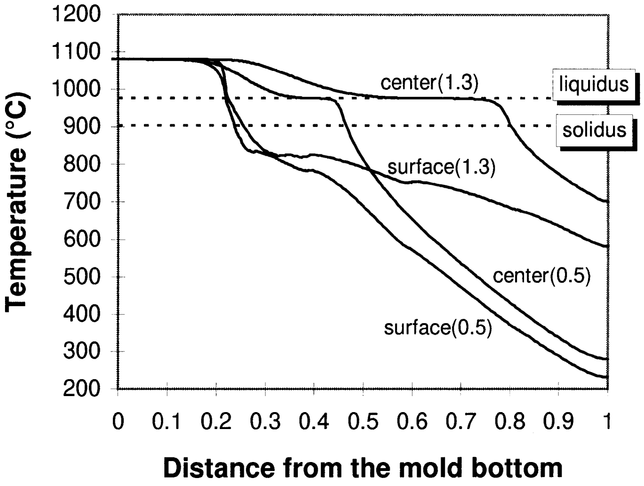

Fig. 37—Center and surface temperatures along the length of the mold for brass 75/25 at casting speeds of 0.5 and 1.3 m/min.

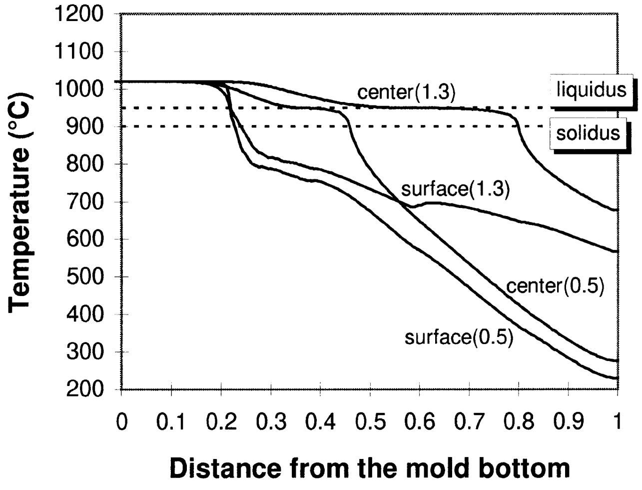

Fig. 38—Center and surface temperatures along the length of the mold for brass 70/30 at casting speeds of 0.5 and 1.3 m/min.

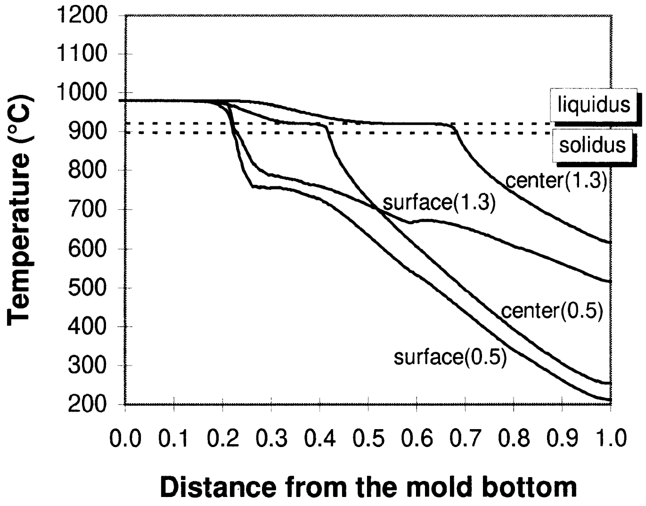

Fig. 39—Center and surface temperatures along the length of the mold for brass 65/35 at casting speeds of 0.5 and 1.3 m/min.

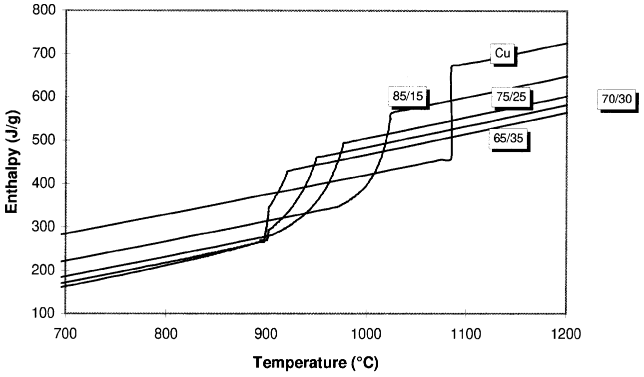

Fig. 40—Calculated enthalpy of copper and the brasses as a function of temperature.

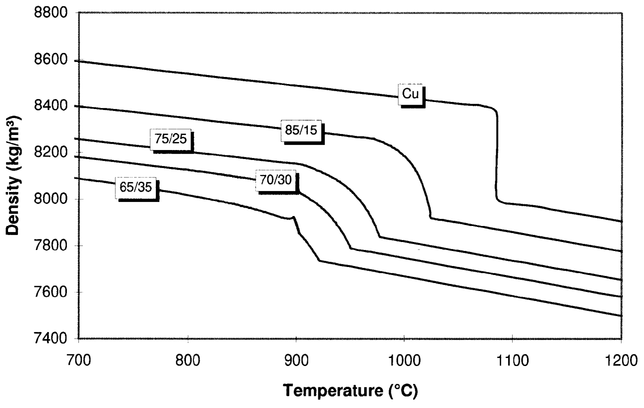

Fig. 41—Calculated density of copper and the brasses as a function of temperature.

70/30 and 65/35, the situation is different, as the solute diffusion in the solid bcc phase is extremely good,[29] and so the solidus temperatures are close to the equilibrium solidus temperatures. At the solidus temperature of brass 70/30, the average bcc phase fraction is approximately 0.21, and for brass 65/35, it is approximately 0.68 (Figure 43). Also, the formation of lattice defects during solidification[10,36] can lead to lower solidus temperatures than expected from the equilibrium solidification.

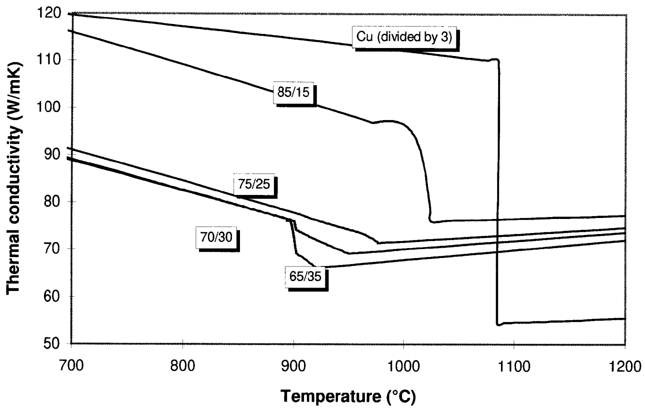

Fig. 42—Calculated thermal conductivity of copper and the brasses as a function of temperature.

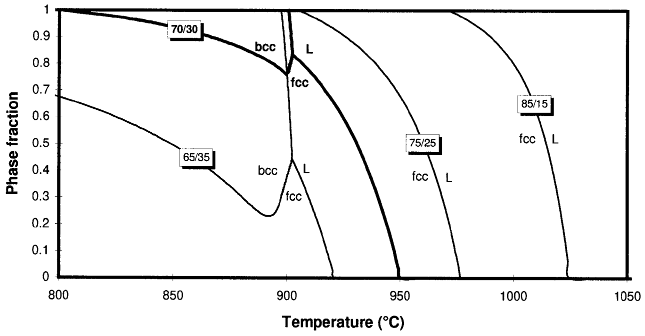

Fig. 43—Phase distribution of the brasses as a function of temperature.

The solidification cooling rate at the mushy zone changes significantly in the cast rod from the surface to the centerline. The cooling rate is very high at the surface of the solidifying rod, and it decreases rapidly toward the center of the rod. An average solidification cooling rate for the entire mushy zone was an input value for calculating material data with the MDM model. The average cooling rates varied between 50 to 100 K/s in the different cases, when neglecting the intermediate cooling rate at the rod surface.

3. *Model for MDM*

The primary aim of the MDM model was to produce thermophysical material data, *i.e.*, enthalpy, density, and thermal conductivity, needed in the calculations of the HTR model. It was also used to predict certain microstructural properties in the cast rods, such as the secondary dendrite arm spacing, the phase distribution, and the microsegregation of zinc.

Calculated enthalpy functions, density functions, thermal conductivity functions, and phase fractions for copper and brasses 85/15, 75/25, 70/30, and 65/35, cooled at an average rate of 70 K/s, have been illustrated in Figures 40 through 43. The data applied in these calculations are given in Table II and Table A1 of Appendix A.

The calculated enthalpy functions of the studied brasses are presented in Figure 40. The higher the zinc content of the alloy, the smaller the total enthalpy change in the mushy zone (including the latent heat of solidification) remains. Applying the classical method for the calculation of the latent heat of solidification by means of Gibbs energy data,[37] the following values were obtained for pure Cu and the studied alloys: L = 208.7 J/g for pure Cu, L = 191.4

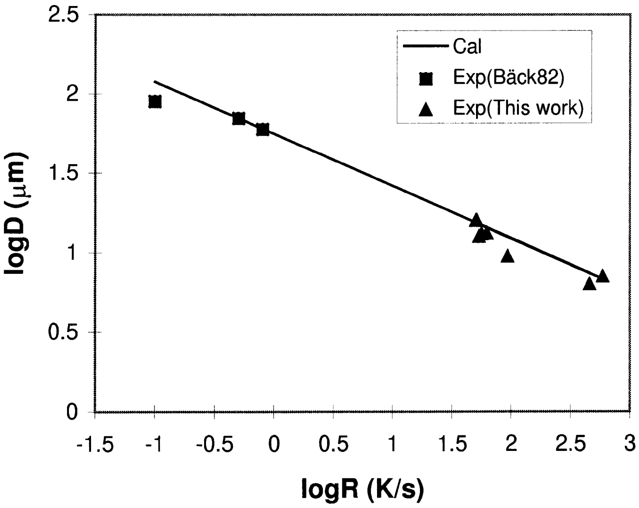

Fig. 44—Dendrite arm spacing at different cooling rates measured in brass 67/33 and 65/35.

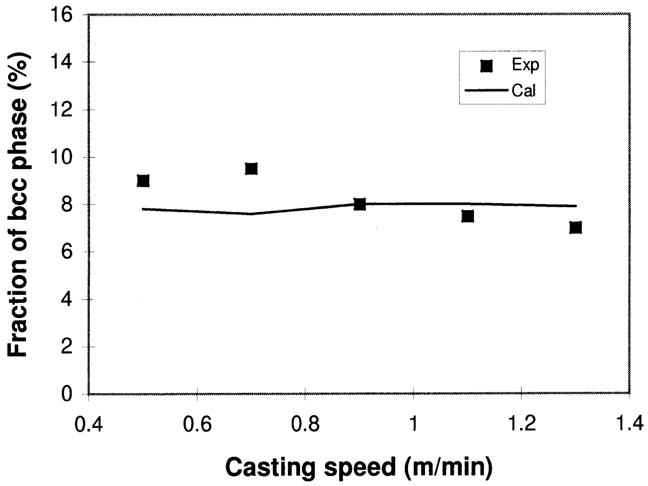

Fig. 45—Comparison of calculated and measured fractions of the bcc phase in brass 65/35 at room temperature.

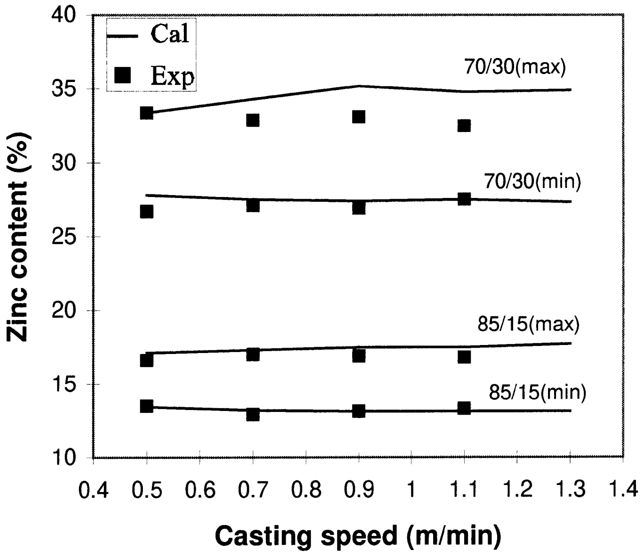

Fig. 46—Comparison of calculated and measured microsegregations (maximum and minimum compositions) of zinc in brasses 85/15 and 70/30.

J/g for brass 85/15, L = 179.2 J/g for brass 75/25, L = 167.9 J/g for brass 70/30, and L = 153.2 J/g for brass 65/35.

Figure 41 shows the calculated density functions. The higher the zinc content of the alloy, the lower the density value of that alloy. On the basis of these density data, one can estimate the relative contraction of the mushy zone as $\beta(\text{pct}) = 100[1 - \rho(T_L)/\rho(T_S)]$, where $\rho(T_L)$ is the density at the liquidus temperature T_L and $\rho(T_S)$ is the density at the solidus temperature T_S. The following values were obtained for pure Cu and the studied alloys: $\beta(\text{pct}) = 4.71$ for pure Cu,$\beta(\text{pct}) = 4.15$ for brass 85/15, $\beta(\text{pct}) = 3.81$ for brass 75/25, $\beta(\text{pct}) = 3.20$ for brass 70/30, and $\beta(\text{pct}) = 2.37$ for brass 65/35, showing that the higher the Zn content of the alloy, the smaller the relative contraction of the mushy zone.

The calculated thermal conductivity functions are illustrated in Figure 42. As can be seen, the zinc alloying decreases the thermal conductivity, especially that of the solid phase. On the other hand, the original data for solid brasses were limited to the room temperature data, and their temperature dependency was adopted from the measurements for pure copper only. Notice that in Figure 42, the thermal conductivity of copper has been divided by three in order to show it with the thermal conductivities of the brasses in the same figure.

Figure 43 shows the solidification paths of the studied brasses. In all of them, the primary solidifying phase is fcc. Brasses 70/30 and 65/35, in addition, undergo a peritectic transformation at a temperature close to 900 °C. This transformation is soon completed, due to the rapid growth of the bcc phase. After the liquid has disappeared, the interdendritic composition soon decreases due to the high diffusivity in the bcc phase, and because of the increasing interface composition $x_{\text{Zn}}{}^{\text{bcc}}$ with the decreasing temperature (Figure 3), the value of the gradient $(dx_{\text{Zn}}/df)^{\text{bcc/fcc}}$ finally changes its sign from positive to negative. This suppresses the growth of the bcc phase toward the fcc phase and forces the bcc/fcc interface to migrate backward, toward the bcc phase (*i.e.*, the sign of term $\Delta f^{\text{bcc/fcc}}$ changes from negative to positive). This happens in a narrow temperature range below the solidus temperature, as shown in Figure 43.

Figure 44 shows the dendrite arm spacings at different cooling rates measured in brasses 67/33[38] and 65/35 (this work). These data were used to optimize the following relation between the dendrite arm spacing d_2 (in μm) and cooling rate $\dot{T}$ (in K/s):

$$d_2 = 56(\dot{T})^{-0.33} \qquad [23]$$

Equation [23] was applied in the calculations of the MDM model. The cooling rate in Eq.[23] refers to the average cooling rate in the mushy zone region.

For the validation of the MDM model, some calculated results for bcc phase fractions and microsegregations of zinc were compared with the measured data. Figure 45 shows the correlation between the calculated and the measured amount of the bcc phase in brass 65/35 at room temperature. The agreement is quite good.

Finally, Figures 46 and 47 show a correlation between the calculated and measured microsegregations of zinc in the cast brasses. Here, the microsegregation is determined

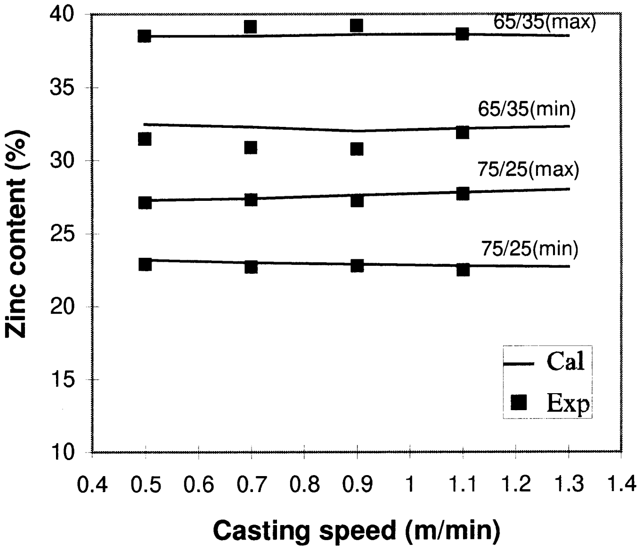

Fig. 47—Comparison of calculated and measured microsegregations (maximum and minimum compositions) of zinc in brasses 75/25 and 65/35.

by means of the average maximum and minimum zinc contents in the structure. The maximum zinc content is found in the interdendritic region, caused by the enrichment of zinc in the liquid, and the minimum zinc content is found in the dendrite arm axis impoverished of zinc. In brass 65/35, where the structure also contained bcc phase, the maximum zinc content was determined as

$$C_{\text{Zn}}^{\text{max}} = f^{\text{fcc}}\, C_{\text{Zn}}^{\text{fcc,max}} + f^{\text{bcc}}\, C_{\text{Zn}}^{\text{bcc}} \qquad [24]$$

where f^{fcc} and f^{bcc} are the fractions of fcc and bcc phases, $C_{\text{Zn}}^{\text{fcc,max}}$ is the maximum zinc content in the fcc phase, and $C_{\text{Zn}}^{\text{bcc}}$ is the zinc content in the bcc phase (composition almost uniform due to high diffusivity in the bcc phase). As can be seen from Figures 46 and 47, the agreement is quite satisfactory. In the case of Figures 45 through 47, it is worth noticing that both the calculated and the experimental results are almost independent of the casting speed.

VII. DISCUSSION

The basic idea of the present study was to establish knowledge of heat transfer and solidification in the mold of the upcasting device for copper and various brasses. For the first time ever, very accurate temperature measurements were carried out in the copper mold on an operating casting machine, and these temperature measurements were used in the mathematical models for heat transfer and solidification simulations.

A. *Mold Temperature Measurements*

Temperature measurements made in the copper jacket of the mold are presented in Section VI–A. The thermocouple instrumentation of the mold wall was difficult due to the small dimensions of the upcast mold and the high measuring accuracy required. Several trials were needed before finding the best positions and optimum number of thermocouples inserted in the mold.

The thermal field of the mold is a function of the heat flux to the mold from the solidifying rod, the efficiency of heat extraction of the mold cooling water, and the thermophysical properties of the mold. The cold side temperature profile is important, since it gives an indication of the possible boiling of the cooling water. The highest temperatures, measured at the cooling water side of the mold, were between 90 °C and 105 °C, the lowest being for brass 65/35 and the highest for copper. The temperature of the intermediate surface of the copper mold is slightly lower than these temperatures and, with the cooling water flow rate of 25 L/min, the mold wall temperature is lower than the boiling temperature of water. An increase in the casting speed shifts up the temperature profiles of the mold quite uniformly, and so an increase in the casting speed above 1.3 m/min will also increase the cold face temperature profile. The increase in the mold wall temperature above the boiling temperature of the cooling water can cause local nucleate boiling in the cooling water. The increasing flow velocity of the cooling water decreases the mold wall temperature, and thus eliminates the nucleate boiling.

With increasing zinc content of the alloy, the temperature profiles of the mold were lowered. The temperatures were lower with increasing zinc content, mainly due to the lower thermal conductivity, lower casting temperature, and smaller enthalpy of the alloys with higher zinc content.

B. *Cooling Water Measurements*

The temperatures of the outgoing cooling water were measured for brasses using a fixed water flow rate of 25 L/min, and for copper castings, the water flow rate was changed from 20 to 25 L/min. The heat amount extracted from the different cast materials is presented in Section VI–B.

The heat extraction increased with decreasing water flow rate, which indicates boiling of the cooling water. The bubble formation needs a lot of energy, and so the heat transfer is increased when the cooling water is boiling. The heat transfer will decrease again if the mold wall temperature rises, so that the bubbles form a continuous vapor film at the copper mold interface, which then acts as a thermal insulator.

The temperature field in the mold can change over time if hysteresis effects related to the nucleation of vapor bubbles take hold. Under these conditions, an increase in the wall temperature is required to initiate boiling, which then also increases the local heat transfer coefficient. This makes the wall temperature drop, and boiling then ceases, subsequently reducing the heat transfer coefficient. Thus, the temperature rises again and the cycle is repeated. This leads to a time-dependent, uneven heat transfer, which is difficult to control and is therefore undesirable. The increasing flow velocity of the cooling water decreases the mold wall temperature and thus eliminates the nucleate boiling. Consequently, a better steady-state situation can be achieved.

C. *Metallographic Analysis*

The metallographic analyses performed are presented in Section VI–C. With increasing casting speed, the orientation of the columnar grains was changed from an axial/radial direction to a more radial direction. As the columnar grains tend to grow toward the main heat flux, it

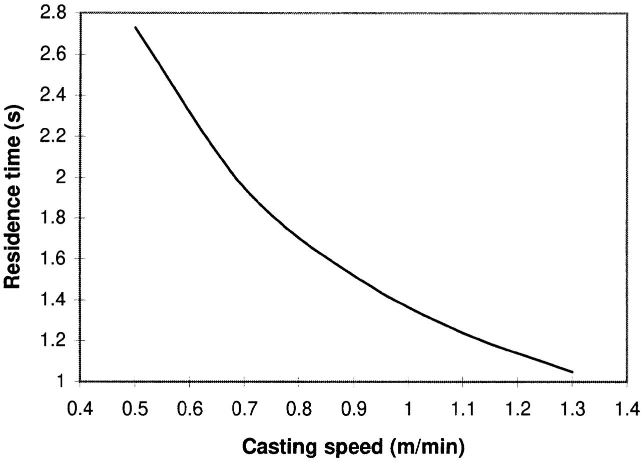

Fig. 48—Residence time at the temperature range of T_{solidus}-1000 K as a function of the casting speed for copper.

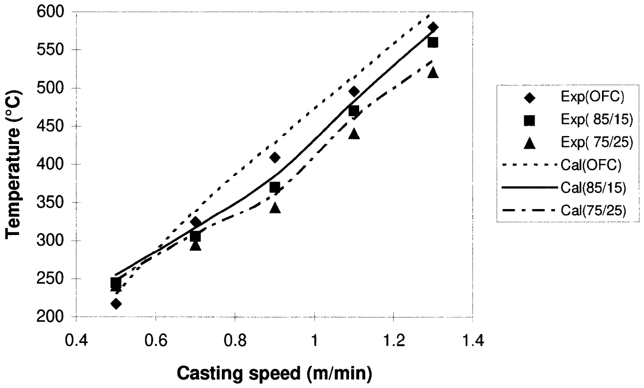

Fig. 49—Comparison of calculated and measured surface temperatures of the cast rod materials at the exit of the mold.

was clear that the heat flux in the mushy zone was more in the radial direction at higher casting speeds. Observing the 0.5 m/min casting examples revealed that, with increasing zinc content, the orientation of the columnar grains tends to change to a more radial direction. This could be explained by the lower thermal conductivity of the cast materials containing more zinc. The heat transfer along the casting direction decreased with increasing zinc content.

The average grain size becomes smaller with increasing casting speed, as the grains have a shorter time to grow at high temperatures just below the solidus temperature. Figure 48 shows the residence time at the temperature range of T_{solidus}-1000 K as a function of the casting speed for copper.

Small equiaxed grains tend to nucleate on the mold surface where nucleation sites are found. No center equiaxed structure was found, as there was insufficient undercooling for a homogeneous nucleation, due to the high superheats used.

The results of the phase distribution showed that brass 65/35 contained some bcc phase in the fcc matrix, whereas the other brasses had a pure fcc structure with no bcc phase. These observations were verified by the MDM model calculations.

D. *Mold Model*

Simulations of the 3-D mathematical model are presented in Section VI–D. A very intensive heat flux was observed in the bottom part of the mold, where the solidification occurs over a short distance, releasing the latent heat. The heat transfer is very good when the metal shell is in contact with the mold and the air gap has not yet formed. Very soon, above the first contact point between the copper mold and graphite die, the partly solidified rod pulls away from the mold wall, creating an air gap that causes a drastic reduction in the heat flux. The overall heat flux decreased with increasing zinc content. This was mainly due to the lower thermal conductivity, lower casting temperature, and smaller enthalpy with higher zinc content. The initial solidification is very rapid due to the very high heat fluxes in the bottom part of the mold. Thus, the air gap formation starts approximately at the same place with all cast materials, and the increase in the casting speed shifts the location of the air gap formation only slightly upward.

In order to increase the heat flux in the mold, several possibilities are available. Increased pressure between the cast rod and the mold has been shown to increase the heat transfer across the metal-mold interface.[18] Consequently, the mold should be placed as deep as possible under the melt level, in order to increase the metallostatic pressure. The higher metallostatic pressure also presses the solidified metal skin against the mold wall for a longer time and so the contact area of the cast rod and mold increases. Furthermore, the right mold taper reduces the air gap width between the cast rod and the mold. The total thermal conductivity of the air gap can be divided into laminar and turbulent thermal conductivity terms. The laminar thermal conductivity can be increased by selecting an intermediate agent, which has a better thermal conductivity value than air. The turbulent thermal conductivity can be increased with higher turbulence in the air gap, which means greater movement of the intermediate agent in the air gap.

E. *Rod Model*

The results of the axisymmetric rod model, which was used to simulate the heat transfer and solidification in the cast rod, are presented in Section VI–D. The surface temperature of the cast rod was measured for copper and brasses 85/15 and 75/25 by attaching two thermocouples to the surface of the rods (Figure 5). The calculated surface temperatures at the mold exit are compared with the measured temperature values in Figure 49. As can be seen from Figure 49, the agreement between the experimental and the calculated temperature values is quite good. However, the simulated surface temperature values are, in all cases, 5 °C to 15 °C higher than the experimental values. This temperature difference may originate from the fact that, with high cooling rates, the latent heat released during solidification can be lower than expected on the basis of the tabulated thermodynamic data. This decrease in the latent heat can be explained by the formation of lattice defects during solidification.[10,36] When lattice defects are formed, the free energy of the solid increases in proportion to the amount and type of defects. Each defect formed during the solidification increases the enthalpy of the solid, and thus, the latent heat will decrease. If the latent heat used in the HTR model simulations is too high, the model will also predict higher surface temperatures than the experimentally measured ones.

For very exact solidification front calculations, the material data should be calculated for each calculation element individually, as the material properties are cooling rate dependent and the cooling rates differ greatly between the cast rod surface and the center in the mushy zone. In these simulations, an average cooling rate was used in the MDM model calculations, which can cause a small error in the solidus and liquidus front shapes.

One can notice from Figures 35 through 39 that solidification of the cast rod shell always begins at the same place, just above the first contact point between the copper mold and the graphite die. This is a specific property of the mold design used in the experiments. A higher casting speed moves the solidification front upward. Therefore, increasing the casting speed too much can lead to a situation where the cast rod has not entirely solidified in the mold and the cast rod will break. Figure 31 shows the distance of the solidus front from the first contact point between the copper mold and the graphite die for copper and the brasses, at different casting speeds. As can be seen, increasing the casting speed increases the distance quite linearly. From a linear approximation of the increase in the solidus front height, a maximum casting speed can be calculated for all the cast materials. If the cast rod should be fully solidified in the mold, the maximum casting speeds would be between 2.2 and 2.5 m/min for the brasses and 5 m/min for copper. The solidification front length corresponds well with the thermal conductivity values and the superheats of the castings concerned. Higher superheats and lower thermal conductivities increase the length of the solidification crater.

The thin solid skin of the cast rod can, however, tear very easily and prevent higher casting speeds. To minimize excessive friction between the cast metal and the mold during casting, a lubricant could be provided between the cast rod and the mold, which would also increase the thermal conductivity of the air gap formed between the cast rod and the mold.

F. *Model for MDM*

The primary aim of the MDM model was to produce thermophysical material data. It was also used to predict certain microstructural properties in the cast rods. The results for the MDM model are presented in Section VI–D.

The calculated microstructural properties were compared with the measured ones in Section VI–D, showing good agreement. It is worth noting that the results concerning the bcc phase fractions in brass 65/35 and the microsegrecation of zinc in all the brasses were quite independent of the casting speed. This can be explained by means of the dendrite arm spacing and cooling rate relationship of Eq. [23] and the cooling histories evaluated from the slopes of the curves of Figures 35 through 39, after dividing the cooler length coordinate values by the casting speed. From the data of Figures 35 through 39, it can be noticed that at the rod surface, the cooling rate is highest for the highest casting speed of 1.3 m/min and lowest for the lowest casting speed of 0.5 m/min. This should lead to a higher microsegregation of zinc at higher casting speeds. According to Eq. [23], however, the higher cooling rate also leads to a finer dendritic structure, improving the homogenization of zinc in the dendrite arms. As a result, the final microsecregation remains at the same level, regardless of the casting speed (Figures 46 and 47).

It is worth remembering that the MDM model pays no attention to the solute accumulation ahead of the advancing dendrite tips. Noticeable accumulation will happen whenever the growth rate of the dendrite tips is sufficiently high, as in the case of this study (calculated rates about 0.45 cm/s). Consequently, the MDM model cannot take into account the resulting undercooling, which, depending on its degree, will cause some error in the calculations of the MDM model. Therefore, a theoretical estimation was made to show the degree of undercooling in the present upcasting process. This has been presented in Appendix B. The resulting undercoolings ranged from 4 °C to 6 °C, so that the higher the zinc content of the brass, the higher the undercooling. Consequently, the real liquidus temperatures would be 4 °C to 6 °C lower than the liquidus temperatures predicted by the MDM model. This causes some deviation in all the calculated results of the study, but, evidently, the effect is quite small.

VIII. CONCLUSIONS

The aim of the study was to provide a comprehensive insight into the heat transfer and solidification phenomena in the mold of the upcasting device for copper and brasses. For the first time, very accurate temperature measurements were carried out in the copper mold on an operating casting machine. The temperature measurements were converted into heat fluxes in the mold with a mathematical model of the mold. These heat fluxes were used as boundary conditions for the cast rod model in the heat transfer and solidification calculations. The material data needed in these calculations were calculated with a model for material data and microstructure. The validation of the models was stated by comparing the calculated results with the experimental ones.

The following conclusions can be drawn from the present study.

1. The mold temperatures and heat flux in the mold decrease with higher zinc content in the alloy, as well as the total heat flux transferred from the cast rod into the cooling water. This was due to the lower thermal conductivity, lower casting temperature, and smaller enthalpy with higher zinc content.
2. Decreasing the cooling water flow rate from 25 to 20 L/min increased the total heat amount transferred from the cast rod into the cooling water. This is assumed to indicate nucleate boiling of the cooling water. The nucleation of bubbles needs a lot of energy and so the heat transfer is increased when boiling of cooling water takes place. This leads, however, to a time-dependent, uneven heat transfer, which is difficult to control.
3. In the upcasting mold, the maximum temperature and heat flux in the copper mold wall were achieved at the first contact point between the copper mold and the graphite die; above this point, they drop to a much lower value along the length of the mold. The heat transfer is extremely good when the metal shell is in contact with

the mold and the air gap has not yet formed. Very soon, above the first contact point between the copper mold and the graphite die, the partly solidified rod pulls away from the mold wall, creating an air gap, which causes a drastic reduction in the heat flux. Solidification of the cast rod shell begins, in all cases, at the first contact point of the copper mold and the graphite die.

4. The height of the liquid pool is increased with increasing superheat and decreasing thermal conductivity, which were examined with the developed mathematical model.
5. With increasing casting speed, the average grain size became smaller and the orientation of the columnar grains was changed from an axial/radial direction to a more radial direction. No center equiaxed structure was found, as there was insufficient undercooling for homogenous nucleation, due to the high superheats used.
6. No macrosegregation of zinc was observed in the cast brass samples. The microsegregation was independent of the casting speed.
7. The calculated surface temperatures of the cast rod at the mold exit agreed well with the measured temperature values. Also, the calculated microstructural properties, such as the secondary dendrite arm spacing, the phase distribution, and the microsegregation of zinc, were compared with the measured ones, showing good agreement.

APPENDIX A

Simulation of phase changes

Conventionally, the phase changes in a dendritic scale are simulated in a volume element set on the side of the dendrite arm.[26] The simulation is made with solute mass balance equation(s) related to the movement of the interfaces and the interfacial compositions changing with decreasing temperature, assuming a complete mixing in the liquid phase. When simulating the phase changes of liquid, fcc, and bcc phases in brasses, the calculations are made stepwise by decreasing the temperature with small temperature increments ΔT as $T = T - \Delta\, T$, and at each temperature, the interfacial compositions are solved with the following chemical-potential-equality equations:

$$\mu^{\phi 1}_{\mathrm{Cu}}\,(T, x^{\phi 1}_{\mathrm{Zn}}) = \mu^{\phi 2}_{\mathrm{Cu}}\,(T, x^{\phi 2}_{\mathrm{Zn}}) \qquad [\mathrm{A1}]$$

$$\mu^{\phi 1}_{\mathrm{Zn}}\,(T, x^{\phi 1}_{\mathrm{Zn}}) = \mu^{\phi 2}_{\mathrm{Zn}}\,(T, x^{\phi 2}_{\mathrm{Zn}}) \qquad [\mathrm{A2}]$$

where $\mu_{\mathrm{Cu}}{}^{\phi}$ and $\mu_{\mathrm{Zn}}{}^{\phi}$ are the chemical potentials of Cu and Zn in phase ϕ (ϕ = L, fcc, bcc) defined according to the substitutional solution model as

$$\begin{aligned}\mu^{\phi}_{\mathrm{Cu}} = {} & ({}^{0}G^{\phi}_{\mathrm{Cu}} - H^{\mathrm{SER}}_{\mathrm{Cu}}) + \mathrm{R}T \ln (1 - x^{\phi}_{\mathrm{Zn}}) \\ & + x^{\phi}_{\mathrm{Zn}}{}^{2}\, {}^{0}L^{\phi}_{\mathrm{CuZn}} + \\ & + (3x^{\phi}_{\mathrm{Zn}}{}^{2} - 4x^{\phi}_{\mathrm{Zn}}{}^{3})\, {}^{1}L^{\phi}_{\mathrm{CuZn}} \\ & + (5x^{\phi}_{\mathrm{Zn}}{}^{2} - 16x^{\phi}_{\mathrm{Zn}}{}^{3} + 12x^{\phi}_{\mathrm{Zn}}{}^{4})\, {}^{2}L^{\phi}_{\mathrm{CuZn}}\end{aligned} \qquad [\mathrm{A3}]$$

$$\begin{aligned}\mu^{\phi}_{\mathrm{Zn}} = {} & ({}^{0}G^{\phi}_{\mathrm{Zn}} - H^{\mathrm{SER}}_{\mathrm{Zn}}) + \mathrm{R}T \ln x^{\phi}_{\mathrm{Zn}} \\ & + (1 - 2x^{\phi}_{\mathrm{Zn}} + x^{\phi}_{\mathrm{Zn}}{}^{2})\, {}^{0}L^{\phi}_{\mathrm{CuZn}} + \\ & + (1 - 6x^{\phi}_{\mathrm{Zn}} + 9x^{\phi}_{\mathrm{Zn}}{}^{2} - 4x^{\phi}_{\mathrm{Zn}}{}^{3})\, {}^{1}L^{\phi}_{\mathrm{CuZn}} \\ & + (1 - 10x^{\phi}_{\mathrm{Zn}} + 29x^{\phi}_{\mathrm{Zn}}{}^{2} - 32x^{\phi}_{\mathrm{Zn}}{}^{3} \\ & + 12x^{\phi}_{\mathrm{Zn}}{}^{4})\, {}^{2}L^{\phi}_{\mathrm{CuZn}}\end{aligned} \qquad [\mathrm{A4}]$$

The thermodynamic data for calculating the chemical potentials are given in Table A1. The calculations were divided into three regions, L + fcc, L L + fcc, + bcc, and fcc + bcc (Figure A1), as discussed in Sections A through C.

A. *Region L + Fcc*

The first step is to solve the liquids temperature T^{L} and the solid composition $x_{zn^{fcc}}$ of the studied alloys from Eqs. [A1] and [A2] by setting $T = T^{L}$ and $x_{Zn^{L}} = x_{Zn^{nom}}$ in the equations ($x_{Zn^{nom}}$ is the nominal composition of the alloy). After this, temperature is decreased stepwise with increments ΔT, and at each temperature, compositions $x_{\mathrm{Zn}^{\mathrm{fcc}}}$ and $x_{Zn^{\mathrm{L}}}$ of the fcc/L interface are calculated from Eqs. [A1] and [A2], and the movement of the interface is simulated with the following mass balance equation (Figure A1):

$$\begin{aligned}& \Delta f^{\mathrm{fcc}/L}\,(x^{L,0}_{\mathrm{Zn}} - x^{\mathrm{fcc}}_{\mathrm{Zn}}) \\ & \quad = (1 - f^{\mathrm{fcc}} - \Delta f^{\mathrm{fcc}/L})(x^{L}_{\mathrm{Zn}} - x^{L,0}_{\mathrm{Zn}}) + M^{\mathrm{fcc}}_{\mathrm{Zn}}\end{aligned} \qquad [\mathrm{A5}]$$

where parameter $M_{\mathrm{Zn}^{\mathrm{fcc}}}$ describing the amount of Zn leaving the fcc/L interface in phase fcc is expressed as

$$M^{\mathrm{fcc}}_{\mathrm{Zn}} = \frac{4D^{\mathrm{fcc}}\Delta T}{d^{2}\dot{T}} \left(\frac{dx_{\mathrm{Zn}}}{df}\right)^{\mathrm{fcc}/L} \qquad [\mathrm{A6}]$$

In these equations, $\Delta f^{\mathrm{fcc}/L}$ is the fractional movement of fcc/L interface, f^{fcc} is the fraction of fcc, $x_{Zn^{L,0}}$ and $x_{Zn^{L}}$ are the liquid compositions of the fcc/L interface at the previous and the present temperature step, $x_{\mathrm{Zn}^{\mathrm{fcc}}}$ is the fcc composition of the fcc/L interface, D^{fcc} (in cm^{2}/s) is the chemical diffusion coefficient in fcc, ΔT (in K) is the temperature step, d (in cm) is the dendrite arm spacing, $\dot{\mathrm{T}}$ (in K/s) is the cooling rate of the process, and $(dx_{\mathrm{Zn}}/df)^{\mathrm{fcc}/L}$ is the concentration gradient in fcc at the fcc/L interface. After each step, the diffusion in fcc is simulated with an implicite finite difference application of Fick's second law using the time increment $\Delta t = \Delta T/\dot{\mathrm{T}}$. This yields the the concentration gradient $(dx_{\mathrm{Zn}}/df^{\mathrm{fcc}/L}$ for the next temperature step. In addition, the present liquid composition value is set to the old value as $x_{Zn^{L,0}} = X_{Zn^{L}}$, and the fcc fraction is increased as $f^{\mathrm{fcc}} = f^{\mathrm{fcc}} + \Delta f^{\mathrm{fcc}/L}$. If the temperature reaches the peritectic temperature, $T^{p} = 1176$ K, the simulation is removed to region L + fcc + bcc (Chapter B). Otherwise, the solidification is continued in region L + fcc, until, with fcc fraction $f^{\mathrm{fcc}} = 1$, one has reached the nonequilibrium solidus temperature and the solidification is ended.

When applying Eq. [A6], one has to know the values for parameters D^{fcc} and d. Based on the measured fcc diffusivities in Cu-Zn alloys[29] the following function was optimized for D^{fcc} (in cm^{2}/s) (Figure. A2):

$$D^{\mathrm{fcc}} = 0.078 \cdot \exp\,(11.62 \cdot \bar{x}^{\mathrm{fcc}}_{\mathrm{Zn}}) \cdot \exp\,(-174{,}730/\mathrm{R}T) \qquad [\mathrm{A7}]$$

i.e., with increasing Zn contents, the diffusivity increases (here, $aMx^{\mathrm{fcc}}_{\mathrm{Zn}}$ refers to the average composition of Zn in the fcc phase calculated from the concentration profile). An estimation for the dendrite arm diameter d (in cm) as a function of cooling rate $\dot{\mathrm{T}}$ (in K/s) was obtained from Eq. [23], correlating well with the measured data for brass 63/37/38/ and brass 65/35 of this study, as shown in Figure. 49.

Table A1. Thermodynamic Parameters of Liquid, Fcc, and Bcc Phases of Cu-Zn System[27]

$$\begin{array}{ll}
{}^0G^L_{\mathrm{Cu}} - H^{\mathrm{SER}}_{\mathrm{Cu}} = 5194.4 + 120.9752T - 24.11239T \ln T - 2.65684 \cdot 10^{-3}T^2 + & \\
\quad + 0.12922 \cdot 10^{-6}T^3 + 52478/T - 5.839 \cdot 10^{-21}T^7 & T < 1358 \text{ K} \\
\quad = -46.9 + 173.8837T - 31.38T \ln T & T > 1358 \text{ K}
\end{array}$$

$$\begin{array}{ll}
{}^0G^L_{\mathrm{Zn}} - H^{\mathrm{SER}}_{\mathrm{Zn}} = -128.5 + 108.1769T - 23.7013T \ln T - 1.71203 \cdot 10^{-3}T^2 + & \\
\quad + -1.26496 \cdot 10^{-6}T^3 + -3.5865 \cdot 10^{-19}T^7 & T < 693 \text{ K} \\
\quad = -3620.5 + 161.6087T - 31.38T \ln T & T > 693 \text{ K}
\end{array}$$

$${}^0L^L_{\mathrm{CuZn}} = -40{,}696 + 12.653T$$

$${}^1L^L_{\mathrm{CuZn}} = 4403 - 6.554T$$

$${}^2L^L_{\mathrm{CuZn}} = 7818 - 3.254T$$

$$\begin{array}{ll}
{}^0G^{\mathrm{fcc}}_{\mathrm{Cu}} - H^{\mathrm{SER}}_{\mathrm{Cu}} = -7770.5 + 130.4854T - 24.11239T \ln T - 2.65684 \cdot 10^{-3}T^2 + & \\
\quad + 0.12922 \cdot 10^{-6}T^3 + 52{,}478/T & T < 1358 \text{ K} \\
\quad = -13{,}542.3 + 183.8042T - 31.38T \ln T + 3.64643 \cdot 10^{29}T^{-9} & T > 1358 \text{ K}
\end{array}$$

$$\begin{array}{ll}
{}^0G^{\mathrm{fcc}}_{\mathrm{Zn}} - H^{\mathrm{SER}}_{\mathrm{Zn}} = -4316.0 + 116.8996T - 23.7013T \ln T - 1.71{,}203 \cdot 10^{-3}T^2 - 1.26496 \cdot 10^{-6}T^3 & T < 693 \text{ K} \\
\quad = -8100.8 + 170.7752T - 31.38T \ln T + 4.70657 \cdot 10^{26}T^{-9} & T > 693 \text{ K}
\end{array}$$

$${}^0L^{\mathrm{fcc}}_{\mathrm{CuZn}} = -42{,}804 + 10.023T$$

$${}^1L^{\mathrm{fcc}}_{\mathrm{CuZn}} = 2936 - 3.053T$$

$${}^2L^{\mathrm{fcc}}_{\mathrm{CuZn}} = 9034 - 5.393T$$

$$\begin{array}{ll}
{}^0G^{\mathrm{bcc}}_{\mathrm{Cu}} - H^{\mathrm{SER}}_{\mathrm{Cu}} = -3753.5 + 129.2304T - 24.11239T \ln T - 2.65684 \cdot 10^{-3}T^2 + & \\
\quad + 0.12922 \cdot 10^{-6}T^3 + 52478/T & T < 1358 \text{ K} \\
\quad = -9525.3 + 182.5492T - 31.38T \ln T + 3.64643 \cdot 10^{29}T^{-9} & T > 1358 \text{ K}
\end{array}$$

$$\begin{array}{ll}
{}^0G^{\mathrm{bcc}}_{\mathrm{Zn}} - H^{\mathrm{SER}}_{\mathrm{Zn}} \; -4398.8 + 115.9589T - 23.7013T \ln T - 1.71203 \cdot 10^{-3}T^2 - 1.26496 \cdot 10^{-6}T^3 & T < 693 \text{ K} \\
\quad = -8183.7 + 169.8345T - 31.38T \ln T + 4.70657 \cdot 10^{26}T^{-9} & T > 693 \text{ K}
\end{array}$$

$${}^0L^{\mathrm{bcc}}_{\mathrm{CuZn}} = -51{,}596 + 13.064T$$

$${}^1L^{\mathrm{bcc}}_{\mathrm{CuZn}} = 7562 - 6.454T$$

$${}^2L^{\mathrm{bcc}}_{\mathrm{CuZn}} = 30{,}744 - 29.915T$$

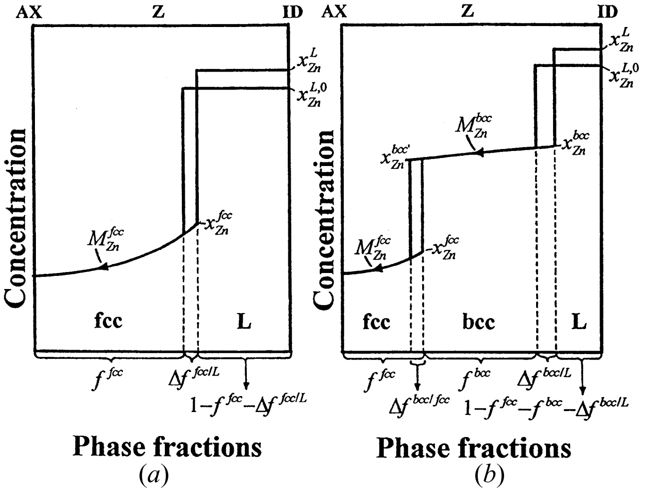

Fig. A1—Composition and phase fraction terms of interfacial material balance equations concerning (*a*) the fcc/L interface in region L + fcc and (*b*) the bcc/L and the bcc/fcc interfaces in region L + fcc + bcc.

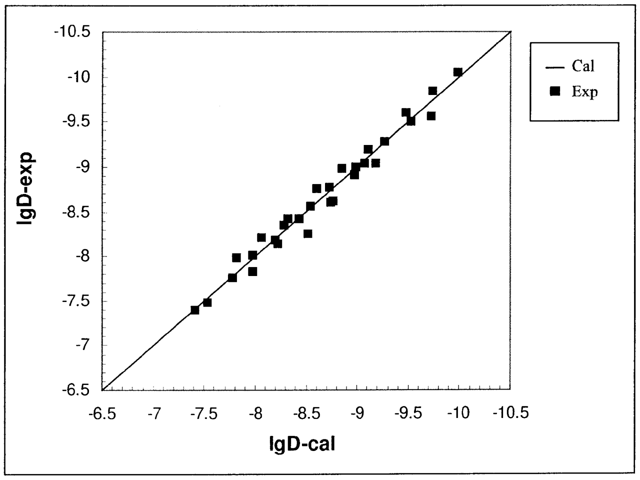

Fig. A2—Calculated *vs* experimental[29] fcc diffusivities in brasses.

B. *Region L + Fcc + Bcc*

In region L + fcc + bcc, temperature is decreased stepwise, Eqs. [A1] and [A2] are applied to calculate compositions $x^{\mathrm{bcc}}_{\mathrm{Zn}}$ and x^L_{Zn} of interface bcc/L and compositions $x^{\mathrm{bcc}'}_{\mathrm{Zn}}$ and $x^{\mathrm{fcc}}_{\mathrm{Zn}}$ of interface bcc/fcc, and the fractional movements of interfaces $\Delta f^{\mathrm{bcc/L}}$ and $\Delta f^{\mathrm{bcc/fcc}}$ are simulated with the following interfacial mass balance equations (Figure. A1(b)):

$$\Delta f^{\mathrm{bcc}/L}\,(x^{L,0}_{\mathrm{Zn}} - x^{\mathrm{bcc}}_{\mathrm{Zn}}) = (1 - f^{\mathrm{fcc}} - f^{\mathrm{bcc}} - \Delta f^{\mathrm{bcc}/L})\,(x^L_{\mathrm{Zn}} - x^{L,0}_{\mathrm{Zn}}) + M^{\mathrm{bcc}}_{\mathrm{Zn}} \quad \text{[A8]}$$

$$\Delta f^{\mathrm{bcc/fcc}}\,(x^{\mathrm{bcc}'}_{\mathrm{Zn}} - x^{\mathrm{fcc}}_{\mathrm{Zn}}) = -M^{\mathrm{bcc}}_{\mathrm{Zn}} + M^{\mathrm{fcc}}_{\mathrm{Zn}} \quad \text{[A9]}$$

where

$$M_{\mathrm{Zn}}^{\mathrm{bcc}} = \frac{4D^{\mathrm{bcc}}\Delta T}{d^2\dot{T}} \frac{x_{\mathrm{Zn}}^{\mathrm{bcc}} - x_{\mathrm{Zn}}^{\mathrm{bcc'}}}{f^{\mathrm{bcc}} + \Delta f^{\mathrm{bcc}/L} - \Delta f^{\mathrm{bcc/fcc}}} \qquad \text{[A10]}$$

$$M_{\mathrm{Zn}}^{\mathrm{fcc}} = \frac{4D^{\mathrm{fcc}}\ \Delta T}{d^2\dot{T}} \left(\frac{dx_{\mathrm{Zn}}}{df}\right)^{\mathrm{fcc/bcc}} \qquad \text{[A11]}$$

In these equations, f^{fcc} and f^{bcc} are the fractions of the fcc and bcc phases, $x_{\mathrm{Zn}^{L,0}}$ and $x_{\mathrm{Zn}^{\mathrm{L}}}$ are the liquid compositions of the bcc/L interface at the previous and the present temperature steps, $x_{\mathrm{Zn}^{\mathrm{bcc}}}$ and $x_{\mathrm{Zn}^{\mathrm{bcc'}}}$ are the bcc compositions of the bcc/L and the bcc/fcc interfaces, $x_{\mathrm{Zn}^{\mathrm{fcc}}}$ is the fcc composition of the bcc/fcc interface, $M_{\mathrm{Zn}^{\mathrm{bcc}}}$ is a parameter describing the amount of Zn leaving the bcc/L interface and entering the bcc/fcc interface in phase bcc, $M_{\mathrm{Zn}^{\mathrm{fcc}}}$ is a parameter describing the amount of Zn leaving the fcc/bcc interface in phase fcc, D^{bcc} (in cm^2/s) is the chemical diffusion coefficient in the bcc phase given as[29]

$$D^{\mathrm{bcc}} = 0.0069 \cdot \exp\left(-78{,}700/\mathrm{R}T\right) \qquad \text{[A12]}$$

and $(dx_{\mathrm{Zn}}/df)^{\mathrm{fcc/bcc}}$ is the concentration gradient in the fcc phase at the bcc/fcc interface. The other terms, D^{fcc}, ΔT, d, and $\dot{\mathrm{T}}$, are explained in Section A. Again, after each temperature step, the diffusion in the fcc phase is simulated with the implicite finite difference application of Fick's second law using the time increment $\Delta t = \Delta T\dot{T}$. This yields the the concentration gradient $(dx_{\mathrm{Zn}}/df)^{\mathrm{fcc/bcc}}$ for the next temperature step. In addition, the present liquid composition value is set to the old value as $x_{\mathrm{Zn}^{L,0}} = x_{\mathrm{Zn}^{L}}$ and the fractions of the fcc and the bcc phases are changed as $f^{\mathrm{fcc}} = f^{\mathrm{fcc}} + \Delta f^{\mathrm{fcc/fcc}}$ and $f^{\mathrm{bcc}} = f^{\mathrm{bcc}} + \Delta f^{\mathrm{bcc}/L} - \Delta f^{\mathrm{bcc/fcc}}$. These calculations are repeated until, with solid fraction $f^{\mathrm{fcc}} + f^{\mathrm{bcc}} = 1$, one has reached the nonequilibrium solidus temperature and the calculations are removed to region fcc + bcc.

Note that in Figure A1(b), the bcc phase grows to both directions, *i.e.*, term $\Delta f^{\mathrm{bcc}/L}$ is positive but term $\Delta f^{\mathrm{bcc/fcc}}$ is negative. This is due to the very high diffusivity in the bcc phase (compare Eq. [A12] to Eq. [A7]). In addition, the high diffusivity in the bcc phase allowed the straight-line approximation for the concentration profile of bcc phase in Fig. A1(b). According to test calculations of bcc diffusion with Fick's second law, only slightly different M^{bcc} terms were obtained for the bcc/L and the bcc/fcc interfaces, whereas in the present treatment, they were assumed to be equal.

C. *Region Fcc + Bcc*

In region fcc + bcc, temperature is decreased stepwise, Eqs. [A1] and [A2] are applied to calculate compositions $x_{\mathrm{Zn}^{\mathrm{bcc}}}$ and $x_{\mathrm{Zn}^{\mathrm{fcc}}}$ of interface bcc/fcc, and the fractional movement of the interface, $\Delta f^{\mathrm{bcc/fcc}}$, is simulated with Eq. [A9], where the term $M_{\mathrm{Zn}^{\mathrm{bcc}}}$ is now given as

$$M_{\mathrm{Zn}}^{\mathrm{bcc}} = \frac{4D^{\mathrm{bcc}}\ \Delta T}{d^2\dot{T}} \left(\frac{dx_{\mathrm{Zn}}}{df}\right)^{\mathrm{bcc/fcc}} \qquad \text{[A13]}$$

Here, term $(dx_{\mathrm{Zn}}/df)^{\mathrm{bcc/fcc}}$ is the concentration gradient in the bcc phase at the bcc/fcc interface obtained in each step by applying the implicite finite difference application of Fick's second law for the diffusion in the bcc phase.

APPENDIX B

Estimation of liquid undercooling

At high growth rates of solidification, it is possible that the solute begins to accumulate ahead of the advancing dendrite tips, leading to the undercooling of the liquid phase. At medium to high growth rates (dendritic regime), one can approximate the undercooling ΔT (in °C) as [26]

$$\Delta T \approx mC_0 \left(1 - \frac{1}{1 - (1 - k)\mathrm{P}}\right) \qquad \text{[B1]}$$

where the Peclet number P is defined as

$$\mathrm{P} \approx \pi \sqrt{\frac{V\Gamma}{-mC_0\ (1 - k)D}} \qquad \text{[B2]}$$

In these equations, C_0 is the nominal composition of solute (in wt pct), m is the liquidus slope (in °C/wt pct), k is the partition coefficient of solute defined as the ratio of solid and liquid composition, V is the growth rate of dendrite tips (in cm/s), Γ is the Gibbs–Thomson coefficient (in cm °C), and D is the diffusion coefficient of solute in liquid (in cm^2/s). When applying Eqs. [B1] and [B2] in the present study, the following parameter values were used: $C_0 = 15$, 25, 30, and 35 wt pct (nominal Zn compositions of the studied alloys), $m = -4.85$ °C/wt pct and $k = 0.85$ (average liquidus slope and partition coefficient for the studied alloys taken from the phase diagram of Figure 3), $V = 0.45$ cm/s (average growth rate of dendrite tips estimated from the temperatures of Figures 35 through 39), $\Gamma = 1.5 \cdot 10^{-5}$ cm °C[26] (value for pure copper melts, but assumed to be valid for Cu-Zn melts also), and $D = 5.10 \cdot 10^{-5}$ cm^2/s (typical value of solute diffusion coefficient in the liquid phase, a measured value for Zn in Cu-Zn melts not available). This resulted in undercoolings from 4 °C to 6 °C for the studied brasses (the higher the Zn content, the higher the undercooling). It is worth remembering that the applied parameter combination given above fulfills the validity condition $P(1 - k) < 1$ of Eqs. [B1] and [B2].

ACKNOWLEDGMENTS

The authors thank Professor Lauri Holappa, Helsinki University of Technology and Outokumpu Copper Products Metal Laboratory (Pori), and the Outokumpu Foundation for financial support.

REFERENCES

1. B. Proctor: *Encyclopedia of Materials Science and Engineering*, 2nd ed., Pergamon Press, Oxford, United Kingdom, 1986, pp. 832-39.
2. S. Pietilä: *Non-Ferrous Wire Handbook*, 3rd ed., Wire Association International Inc., Guilford, CT, 1995, pp. 204-10.
3. R.B. Mahapatra, J.K. Brimacombe, I.V. Samarasekera, N. Walker, E.A. Paterson, and J.D. Young: *Metall. Trans. B*, 1991, vol. 22B, pp. 861-73.
4. R.B. Mahapatra, J.K. Brimacombe, and I.V. Samarasekera: *Metall. Trans. B*, 1991, vol. 22B, pp. 875-88.
5. I.V. Samarasekera, D.L. Anderson, and J.K. Brimacombe: *Metall. Trans. B*, 1982, vol. 13B, pp. 91-104.
6. I.V. Samarasekera and J.K. Brimacombe: *Metall. Trans. B*, 1982, vol. 13B, pp. 105-16.
7. B.G. Thomas: *Steelmaking Conf.*, Iron and Steel Society, Washington, DC, 1991, vol. 74, pp. 105-18.

8. B.G. Thomas, L.M. Mika, and F.M. Najjar: *Metall. Trans. B*, 1990, vol. 21B, pp. 387-400.
9. G. Li and B.G. Thomas: *Metall. Mater. Trans. B*, 1996, vol. 27B, pp. 509-25.
10. C.-M. Raihle, H. Fredriksson, and S. Östlund: *Conf. on Modeling of Casting, Welding and Advanced Solidification Processes VII*, London, 1995, The Minerals, Metals & Materials Society, Warrendale, PA, 1995, pp. 817-24.
11. C.-M. Raihle, P. Sivesson, and H. Fredriksson: *Conf. on Modeling of Casting, Welding and Advanced Solidification Processes VI*, Palm Coast, FL, 1993, The Minerals, Metals & Materials Society, Warrendale, PA, 1993, pp. 577-84.
12. P. Sivesson, C.-M. Raihle, and J. Konttinen: *Mater. Sci. Eng*, 1993, vol. A173 pp. 299-304.
13. C.-M. Raihle, P. Sivesson, M. Tukiainen, and H. Fredriksson: *Ironmaking and Steelmaking*,1994, vol. 21, pp. 487-95.
14. S. Louhenkilpi, E. Laitinen, and R. Nieminen: *Metall. Trans. B*, 1993, vol. 24B, pp. 685-93.
15. S. Louhenkilpi: *Scand. J. Metall.*, 1994, vol. 23, pp. 9-17.
16. H. Natusch: Ph.D. Thesis, University of Siegen, 1995.
17. T.G. O'Connor and J.A. Dantzig: *Metall. Mater. Trans. B*, 1994, vol. 25B, pp. 443-57.
18. J.P. Verwijs and D.C. Weckman: *Metall. Trans. B*, 1988, vol. 19B, pp. 201-12.
19. G. Ogiermann and R. Emmerich: *Metallurgy*, 1986, vol. 1, pp. 22-26.
20. J.-P. Birat, M. Larrecq, J.-Y. Lamant, and J. Petegnief: *Steelmaking Conf.*, Iron and Steel Society, Washington, DC, 1991, Vol. 74, pp. 39-50.
21. K. Härkki and L. Holappa: *Conference on Modelling of Casting, Welding and Advanced Solidification Processes VII*, London, 1995, The Minerals, Metals & Materials Society, Warrendale, PA, 1995, pp. 857-64.
22. K. Härkki and L. Holappa: *4th Int. Colloquium on Process Simulation*, Espoo, 1997, Pica-Set OY, Espoo, Finland, 1997, pp. 139-52.
23. K. Härkki, J. Miettinen, and L. Holappa: *Conf. Numerical Methods for Thermal Problems*, Swansea, United Kingdom, 1997, Pineridge Press Limited, Mumbles, Swansea, U.K., 1997, pp. 496-507.
24. T.B. Massalski: *Binary Alloy Phase Diagrams*, ASM, Metals Park, OH, 1986, p. 981.
25. *FIDAP 7.0 Theory Manual*, Fluid Dynamics International, Evanston, IL, 1993.
26. W. Kurz and D.J. Fisher: *Fundamentals of Solidification*, 3rd ed., Trans Tech Publications, Aedermannsdorf, Switzerland, 1989.
27. M. Kowalski and P.J. Spencer: *J. Phase Equilibria*, 1993, vol. 14, pp. 432-38.
28. Y. Kawai and Y. Shiraishi: *Handbook of Physico-Chemical Properties at High Temperatures*, The Iron and Steel Institute of Japan, 1988.
29. E.A. Brandes and G.B. Brook: *Smithells Metals Reference Book*, 7th ed., Butterworth-Heinemann Ltd., Oxford, United Kingdom, 1992.
30. K.W. Andrews and W. Hume-Rothery: *Proc. R. Soc.*, 1941, vol. A178, pp. 464-73.
31. E.A. Owen and L. Pickup: *Proc. R. Soc.*, 1934, vol. A145, pp. 258-67.
32. W.B. Pearson: *A Handbook of Lattice Spacings and Structures of Metals and Alloys*, Pergamon Press, London, 1958.
33. *Metals Handbook*, 10th ed., ASM INTERNATIONAL, Metals Park, OH, 1990, vol. 2, pp. 346-55.
34. R.C. Weast: *Handbook of Chemistry and Physics*, 53rd ed., The Chemical Rubber Co., Cleveland, OH, 1973.
35. A.T. Dinsdale: *CALPHAD*, 1991, vol. 15, pp. 317-425.
36. S. Berg, J. Dahlström, and J. Fredriksson: *Iron Steel Inst. Jpn. Int.* 1995, vol. 35, pp. 876-85.
37. J. Miettinen: *Metall. Mater. Trans. B*, 1997, vol. 28B, pp. 281-91.
38. L. Bäckerud, L.-M. Liljenvall, and H. Steen: *Solidification Characteristics of Some Copper Alloys*, International Copper Research Association, Inc., Stockholm, Sweden, 1982.